

# **REMOTE SENSING OF EUPHOTIC DEPTH IN LAKE NAIVASHA**

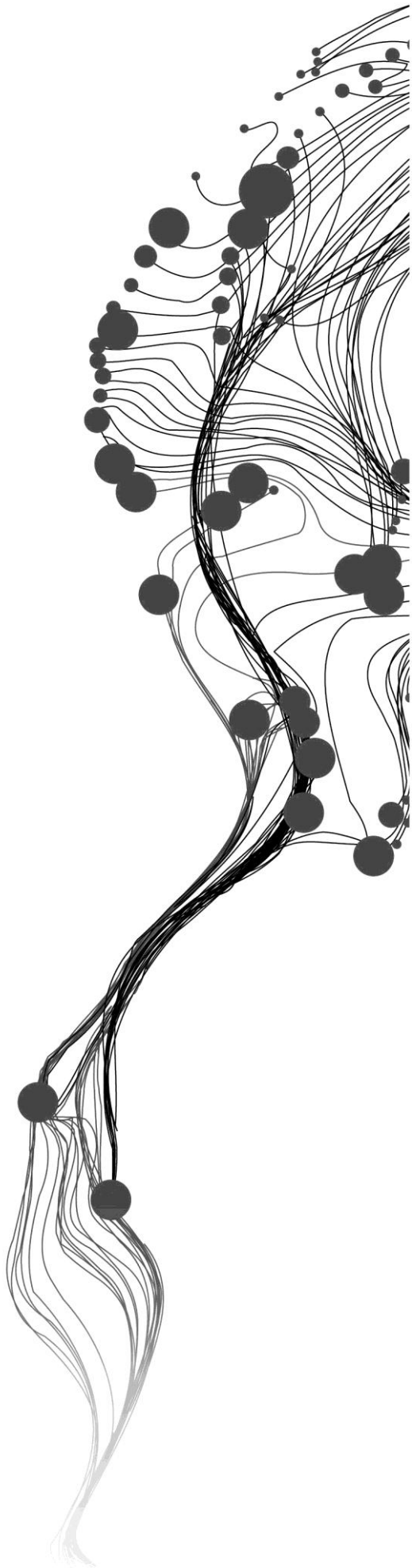
NOBUHLE PATIENCE MAJOZI

February, 2011

SUPERVISORS:

Dr. Ir. Mhd, S, Salama

Prof. Dr. Ing., W, Verhoef



# REMOTE SENSING OF EUPHOTIC DEPTH IN LAKE NAIVASHA

NOBUHLE PATIENCE MAJOZI

Enschede, The Netherlands, February, 2011

Thesis submitted to the Faculty of Geo-Information Science and Earth Observation of the University of Twente in partial fulfilment of the requirements for the degree of Master of Science in Geo-information Science and Earth Observation.

Specialization: Water Resources and Environmental Management

**SUPERVISORS:**

Dr. Ir. Mhd, S., Salama

Prof. Dr. Ing., W., Verhoef

**THESIS ASSESSMENT BOARD:**

Dr. Ir., C.M.M., Mannaerts (Chair)

Dr, D.M., Harper (External Examiner, Department of Biology - University of Leicester – UK)

#### DISCLAIMER

This document describes work undertaken as part of a programme of study at the Faculty of Geo-Information Science and Earth Observation of the University of Twente. All views and opinions expressed therein remain the sole responsibility of the author, and do not necessarily represent those of the Faculty.

## ABSTRACT

Euphotic zone depth is a fundamental measurement of water clarity in water bodies. It is determined by the water constituents like suspended particulate matter, dissolved organic matter, phytoplankton, mineral particles and water molecules, which attenuate solar radiation as it transits down a water column. Primary production is at its maximum within the euphotic zone because there is sufficient Photosynthetically Active Radiation (PAR) for photosynthesis to take place. The study was conducted in Lake Naivasha, Kenya. Rich in biodiversity, it supports a thriving fishery, an intensive flower-growing industry and geothermal power generation, thereby contributing significantly to local and national economic development. Little is known about the optical properties of Lake Naivasha, and remote sensing methods have not been applied to study the water quality status of this lake. Thus the goal of the research was to estimate euphotic depth ( $Z_{eu}$ ) based on attenuation coefficient ( $K_d(\lambda)$ ), using remotely sensed data (MERIS). Ocean optics modelling was based on deriving  $K_d(\lambda)$  from in-situ underwater optical measurements of downwelling irradiance at two depths (0.1 and 0.6m) and remote sensing reflectance ( $R_{rs}(\lambda)$ ). Based on the relationship between  $K_d(\lambda)$  and  $1/R_{rs}(\lambda)$ , the spectra were systemically characterised into three distinct classes: 430-600nm, 600-800nm and 800-930nm. Model coefficients were derived for each spectral range using insitu data. The models successfully reproduced measured  $K_d(\lambda)$  ( $R^2 > 0.87$  and RMSE of 0.97, 0.85 and  $0.26\text{m}^{-1}$ , respectively). A local model was also developed to retrieve  $Z_{eu}$  from  $K_d(620)$ . MERIS match-up data was used to validate the spectral range-based  $K_d(\lambda)$  model. Results gave an RMSE of 0.86, 0.25 and  $2.55\text{m}^{-1}$  respectively. The empirical methods of deriving  $Z_{eu}$  was also applied on  $K_d(490)$  and  $K_d(620)$  products of MERIS, and the  $K_d(620)$  method was more accurate ( $\epsilon = 2.07\%$  and  $\text{RMSE} = 0.044\text{m}$ ). Finally, maps of  $Z_{eu}$  produced revealed that it varies between 0.9 and 1.3m, and that the deepest light penetration is experienced in the Crescent Island part of Lake Naivasha.

## ACKNOWLEDGEMENTS

My sincere gratitude goes to a number of people without whose guidance, assistance, love and support this thesis would not have been a success.

First and foremost, I am indebted to my first supervisor, Suhyb Salama for his unwavering guidance and support throughout this challenging period. I must also include Wouter Verhoef, who as my second supervisor was always open to consultations granting me his vast knowledge and experience about the subject matter.

The European Space Agency (ESA), who provided me with MERIS images to make this research complete- your contribution to this research is appreciated.

My appreciation also goes to the Naivasha community who assisted during my fieldwork. Sarah Higgins, who allowed us to use her premises in order to access the lake, and David Harper for allowing us to use your laboratory to analyse our water samples without any restrictions- your invaluable support during data collection is much appreciated. Naivasha group, you made the burden much lighter at the lake, thank you.

I express my gratitude to the staff from the Water Resources and Environmental Management Department of the ITC Faculty for facilitating an excellent environment to successfully complete my research. To my colleagues, thank you for your camaraderie, for the moments of laughter, celebration and struggles we shared during the course of the study. They will be cherished forever.

My mother and siblings, without your prayers and moral support I would not have come through this challenging and exciting life experience. My friends, I am grateful for your encouragement and support during this journey. Lastly, the Netherlands Fellowship Program for granting me the financial support to pursue my studies at study at ITC.

Glory and honour to the Almighty God for His bountiful mercies that carried me through the course of my study.

# TABLE OF CONTENTS

---

Abstract .....	i
Acknowledgements .....	ii
Table of contents .....	iii
List of figures.....	iv
List of tables .....	v
Acronyms .....	vi
1. Introduction.....	1
1.1. Background.....	1
1.2. Research Problem.....	2
1.3. Research Objectives.....	3
1.4. Thesis outline .....	3
2. Literature Review.....	5
2.1. Euphotic Depth.....	5
2.2. Attenuation Coefficient.....	6
3. Study Area and Datasets.....	9
3.1. Study area.....	9
3.2. Datasets .....	10
4. Methodology.....	15
4.1. Proposed Approach.....	15
4.2. Image Processing.....	18
5. Results.....	21
5.1. In-situ Euphotic depth.....	21
5.2. Attenuation coefficient model calibration and validation .....	23
5.3. Model testing using MERIS match-up data.....	24
6. Discussion.....	29
6.1. Field Data.....	29
6.2. $K_d(\lambda)$ Model Calibration and Validation.....	32
6.3. Mapping $Z_{eu}$ .....	33
6.4. Limitations.....	33
7. Conclusions and Recommendations .....	35
7.1. Conclusions .....	35
7.2. Recommendations.....	35
List of References .....	37

# LIST OF FIGURES

---

Figure 1-1: An illustration of the different lake zones based on light penetration (courtesy of <a href="http://www.aquatic.uoguelph.ca/lakes/page21.htm">http://www.aquatic.uoguelph.ca/lakes/page21.htm</a> ) .....	2
Figure 1-2: The outline of the thesis .....	4
Figure 3-1: Location map of the study area (Source: Aster 2010) .....	9
Figure 3-2: Sampling routes during the field campaign.....	11
Figure 4-1 a, b, c, d: Relationship between $K_d(\lambda)$ and $R_{rs}(\lambda)$ .....	17
Figure 5-1a, b: Spectral $K_d$ and depth of light penetration .....	21
Figure 5-2: the relationship between in-situ derived $K_d(\text{PAR})$ and $Z_{eu}$ .....	22
Figure 5-3 a, b: Correlation between $K_d(\text{PAR})$ and $K_d(490)$ ; $K_d(\text{PAR})$ and $K_d(620)$ .....	22
Figure 5-4 a, b: Comparison of $K_d(\text{PAR})$ -derived to $K_d(490)$ -derived $Z_{eu}$ and $K_d(620)$ -derived $Z_{eu}$ .....	23
Figure 5-5 a, b: Correlation of modelled $Z_{eu}$ to in-situ $K_d(\text{PAR})$ .....	23
Figure 5-6 a, b, c: Comparison between in-situ $K_d(\lambda)$ and modelled $K_d(\lambda)$ based on the spectral regions ...	24
Figure 5-7.3a, b, c, d: Accuracy assessment of atmospheric correction .....	25
Figure 5-8 a, b, c: Graphical comparison of the $K_d(\lambda)$ models on MERIS data to measured $K_d(\lambda)$ .....	26
Figure 5-9: Comparison of MERIS $Z_{eu}$ products derived from $K_d(490)$ and $K_d(620)$ .....	27
Figure 5-10a, b, c, d: Spatial profile of $Z_{eu}$ in the lake- a and c North-South profiles, b and d West-East profiles.....	27
Figure 5-11 a, b, c: Maps showing spatial variation showing spatial variation of $Z_{eu}$ over 7 days (a- 20.09.10; b-23.09.10; c-26.09.10 products), the NS and WE cross-sections are shown in full lines. ....	28
Figure 6-1: Spectral signature of the lake water.....	30
Figure 6-2a, b: the comparison of the general spectral trend between $a(\lambda)$ and $K_d(\lambda)$ - (Figure a taken from Mueller, et al., (2003b)) .....	31
Figure 6-3 a, b: In-situ derived $R_{rs}(\lambda)$ and $K_d(\lambda)$ .....	32

## LIST OF TABLES

---

Table 2-1: An overview of algorithms to derive $K_d(\lambda)$ .....	7
Table 3-1: An overview of the data collected in the field and equipment used .....	11
Table 3-2: Specifications of MERIS Sensor (courtesy of <a href="http://www.brockmann-consult.de/beam">http://www.brockmann-consult.de/beam</a> ) .....	13
Table 3-3: MERIS data match-up sites. ....	13
Table 5-1: Accuracy Assessment of $K_d(\lambda)$ models .....	23
Table 5-2: Statistical analysis of the atmospheric correction of MERIS match-up data.....	25
Table 5-3: Error analysis of $K_d(\lambda)$ model on MERIS data.....	26

## ACRONYMS

$a(\lambda)$	Bulk absorption coefficient	$m^{-1}$
$b_b(\lambda)$	Bulk backscattering coefficient	$m^{-1}$
$K_d(\lambda)$	Attenuation coefficient	$m^{-1}$
$K_w(\lambda)$	attenuation coefficient of pure water	$m^{-1}$
$L_w(\lambda)$	Water-leaving radiance	$Wm^{-2}\mu m^{-1}sr^{-1}$
$E_d(\lambda)$	Downwelling Irradiance	$Wm^{-2}\mu m^{-1}$
PAR	Photosynthetically Active Radiation	$Wm^{-2}\mu m^{-1}sr^{-1}$
$R_{rs}(\lambda)$	Remote Sensing Reflectance	$sr^{-1}$
$Z_{eu}$	Euphotic Zone Depth	$m^{-1}$
$\theta_z$	Solar Zenith Angle	Radians
Chl- <i>a</i>	Chlorophyll- <i>a</i> concentration	$mgm^{-3}$
CDOM	Coloured dissolved organic matter	
NAP	Non-algal particles	
SPM	Suspended particulate matter	
$\epsilon$	Mean Relative Error	%
RMSE	Root Mean Square Error	
$R^2$	R-square	
AC	Atmospheric correction	
CZSZ	Coastal Zone Colour Scanner	
EOLISA	Earth Observation Link-Stand Alone	
ESA	European Space Agency	
FR	Full Resolution	
IOCCG	International Ocean Colour Coordinating Group	
MERIS	Medium Resolution Imaging Spectrometer	
NASA	National Aeronautics and Space Administration	
RR	Reduced Resolution	
SeaWiFS	Sea-viewing Wide Field-of-View Sensor	

# 1. INTRODUCTION

## 1.1. Background

Lake Naivasha is an important source of fresh water in a dry water-scarce zone. Rich in biodiversity, the lake supports a thriving fishery, intensive horticulture and floriculture industries and geothermal power generation. It therefore plays a key role in the local and national economic development. Due to these factors and the quest for socioeconomic development within the lake ecosystem itself as well as other activities within the catchment, it is under enormous anthropogenic pressure (Becht & Chesterton, 2010; Otian'a-Owiti & Abiya Oswe, 2006). All these factors have contributed to the deteriorating water quality status of the lake over time, posing a threat to the aquatic life as evident through a report on the death of the fish in the lake (Kona & Mwiti, 2010). Because of increased input of nutrients like phosphorus and nitrogen over the years, phytoplankton levels have also increased, as such the lake was declared eutrophic (Harper, 1993). Together with increased sediment load being introduced into the lake through Gilgil and Malewa rivers, the turbidity levels have been on the increase over the years.

Monitoring the water quality of the lake is of paramount importance as a foundation for its management and ultimately its sustainability. However, traditional, in-situ monitoring is complex with low spatial and temporal coverage, resulting in inadequate estimates of the lake conditions. The advent of remote sensing techniques, integrated with water bio-optical models and in-situ data, has improved water quality monitoring, as reiterated in the report by Di Giacomo et al. (2007). Remote sensing data are time and cost efficient, provide the opportunity for regular observation of even remote regions, and allow for spatial and temporal investigation of these ecosystems.

Euphotic zone depth,  $Z_{eu}$ , defines the water layer at which the solar radiation diminishes to 1% of its initial value at the surface (Scheffer, 2001). It is a quantitative measure of water clarity, determined by the presence of total suspended material, dissolved coloured matter, as well as water molecules themselves. The net primary production is at its maximum within the euphotic zone as there is sufficient Photosynthetically Active Radiation (PAR) for photosynthesis since the energy fixed by photosynthesis exceeds that lost by respiration; beyond this depth PAR is too low for phytoplankton to maintain a positive net photosynthesis thus they cannot grow (Khanna et al., 2009). Euphotic zone depth is critical for the survival of our freshwater ecosystems as indicated by a study by Bilotta and Brazier (2008) as well for heat and greenhouse gases transfer within the water column. Being a cumulative measure of biogeochemical properties of the water column, Chen et al. (2007) state that variations of euphotic depth depict environmental patterns that might be associated with climate change.

Figure 1-1 shows the different lake zone based on the light penetration. The euphotic zone depth is depicted the photic zone on the illustration.

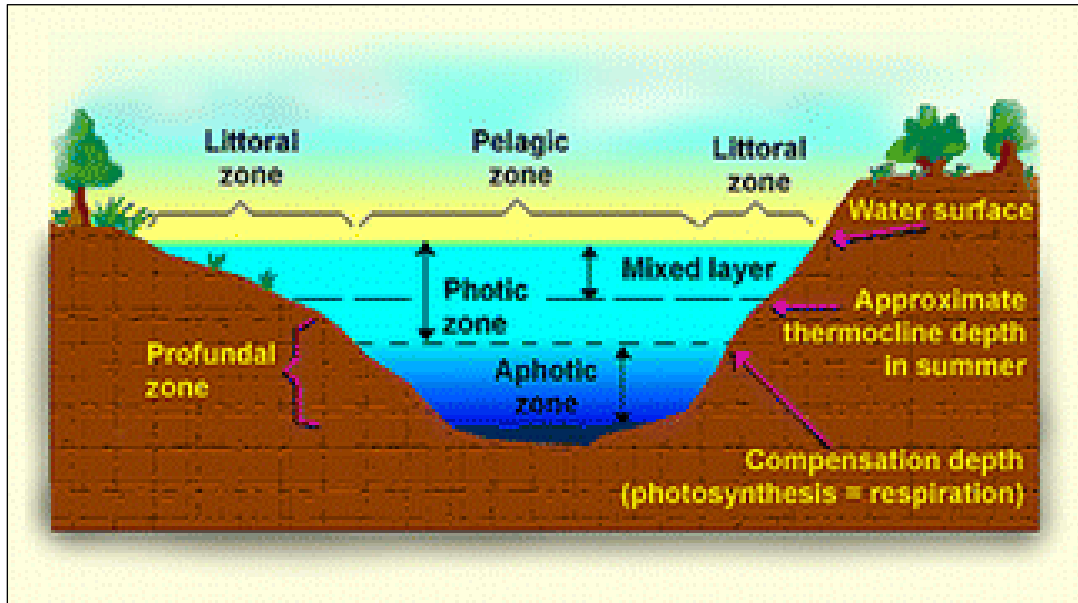


Figure 1-1: An illustration of the different lake zones based on light penetration (courtesy of <http://www.aquatic.uoguelph.ca/lakes/page21.htm>)

Secchi Disk depth and concentrations of water constituents that determine light attenuation, for instance Chl-*a* and SPM, have been employed to compute  $Z_{eu}$  as shown by several studies (Liu et al., 2002). However, these have proven to be unreliable, especially in complex inland waters like Lake Naivasha. This is because in these waters euphotic depth is highly variable depending on such factors as turbidity, supply of nutrients in the water, tidal turbulence, and temperature, for instance, high nutrient levels will encourage a greater biomass of phytoplankton near the surface, which causes shading and consequent reduction in depth of the euphotic zone. Attenuation coefficient,  $K_d(\lambda)$ , on the other hand has demonstrated high accuracy, because of the physical relationship between the two parameters. With the advent of remote sensing techniques, empirical and semi-analytical algorithms have been developed to derive  $K_d(\lambda)$ , as evident in literature (Kratzer et al., 2003; Z. Lee et al., 2007; Tang et al., 2007).

The aim of the study therefore was to derive multispectral attenuation coefficient directly from remote sensing reflectance, and ultimately euphotic depth from attenuation coefficient.  $Z_{eu}$  maps were eventually produced using the Medium Resolution Imaging Spectrometer (MERIS) data where the spatial variation was then analysed.

## 1.2. Research Problem

Euphotic zone depth is a fundamental measurement of water clarity, determined by water constituents like coloured dissolved organic matter (CDOM), phytoplankton, non-algal particles (NAP) and water molecules. These water constituents attenuate the solar radiation as it travels through a water column. A reduced euphotic zone depth means a reduced primary productivity zone for aquatic life; this ultimately leads to a compromised aquatic ecosystem.

Various studies have been carried out to determine and model the water quality status, for instance ecological and chemical status, of Lake Naivasha as highlighted by Becht and Chesterton (2010) in their report. Otian'a-Owiti and Abiya Oswe (2006) also give an overview of the research that has been done on the lake. However, of these methods none has ever investigated, the optical properties of the lake, which define the light status of the lake, in particular light penetration using remote sensing methods. Although

satellite imagery has been used for research on the lake (Fathy et al., 1999), it has not been employed for monitoring its water quality.

The goal of the research, therefore was to examine the light penetration of Lake Naivasha, based on in-situ measurements as well as remote sensing data. Research on remote sensing of  $K_d(\lambda)$  has focussed on modelling diffuse attenuation coefficient a single band at a time Lee, et al., (2005a). Therefore this study went on to develop a model to estimate spectral attenuation coefficient based on the inverse relationship between  $K_d(\lambda)$  and  $R_{rs}(\lambda)$ , and ultimately deriving  $Z_{eu}$  directly from  $K_d(\lambda)$ . Using MERIS data, the spatial variability of euphotic depth was investigated.

### **1.3. Research Objectives**

#### **1.3.1. General Objective**

The objective was to investigate retrieve euphotic depth of Lake Naivasha using remote sensing methods.

#### **1.3.2. Specific Objectives**

- To quantify euphotic depth of the lake using in-situ measurements
- To develop an algorithm to derive multispectral diffuse attenuation coefficient using in-situ radiometric measurements
- To assess the validity of the developed diffuse attenuation model
- To derive euphotic depth of the lake from MERIS data
- To assess the spatial variation of euphotic depth of the lake using MERIS data.

### **1.4. Thesis outline**

The research intended to examine the light penetration of Lake Naivasha, based on insitu measurements as well as remote sensing data. It focussed on developing a model to estimate the attenuation coefficient, and ultimately euphotic depth. Using remote sensing data, the spatial variability of euphotic depth was investigated.

The structure of the thesis is illustrated in Figure 1-2.

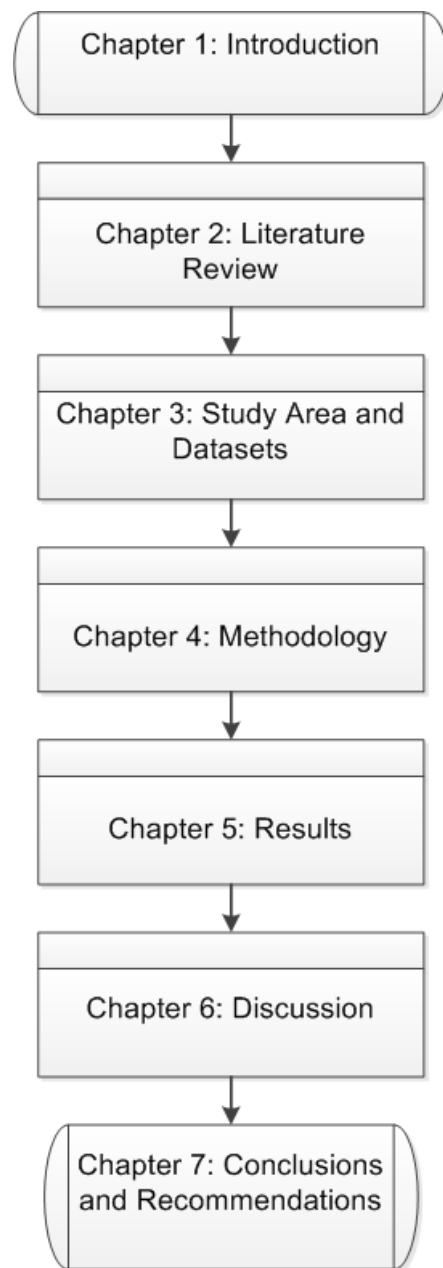


Figure 1-2: The outline of the thesis

## 2. LITERATURE REVIEW

### 2.1. Euphotic Depth

Light, the source of energy for photosynthesis, is one of the limiting factors critical for regulating net primary productivity of water bodies. The Euphotic zone (euphotic meaning ‘well lit’ in Greek) is where there is the greatest primary productivity because photosynthesis occurs within the euphotic depth since there is sufficient PAR, beyond which respiration is greater than net photosynthesis (Kirk, 1994). Various studies (Goosen et al., 1999; Malone, 1987; Platt et al., 1988; Spitzer, 1980) have been carried out to substantiate the relationship between light limitation and ocean primary productivity. Kettle and Merchant (2008) also illustrated in their model that as the water column depth increases, a decrease of chlorophyll is witnessed. Khanna et al., (2009) went on to point out that the greater the ratio of euphotic depth to depth of mixing, the higher the photosynthesis rate, indicating growth of phytoplankton within the euphotic zone.

Considering that CO<sub>2</sub> is used and O<sub>2</sub> is a by-product during the process of photosynthesis, the euphotic zone is also significant for the transfer of greenhouse gases, primarily CO<sub>2</sub> and O<sub>2</sub> (Schwartz et al., 2002). The euphotic depth governs the distribution of heat in the surface. Kahru et al. (1993) in their research demonstrated that surface accumulations of filamentous algal blooms cause an increase in the satellite-derived sea surface temperature by up to 1.5°C. They attributed this phenomenon to increased absorption of sunlight due to increased phytoplankton pigment concentration. Also since primary producers are found within the euphotic zone, approximately 90% of all aquatic life lives within this depth.

Euphotic depth is derived directly from the attenuation coefficient ( $K_d(\lambda)$ ) based on Beer Lambert’s Law. Secchi disk depth has also been used as a conventional oceanographic survey method of estimating water transparency and euphotic depth. However, Secchi depth is a qualitative, less reliable measurement dependent on experience and eyesight of the viewer among other factors.

A method was developed by Morel and Berthon (1989) based on the relationship that links euphotic depth to the total chlorophyll pigment content within the euphotic layer. The method involved progressively integrating the chlorophyll pigment values until the last  $Z_{eu}$  value becomes lower than the depth used when integrating the profile. When this happens the process is stopped and reversed for validation, followed by an iterative scheme that allows the exact  $Z_{eu}$  to be determined by interpolation. Krazter et al. (2003) investigated the relationship between  $K_d(490)$  and  $K_d(PAR)$  using in-situ measurements by employing linear regression analysis and came up with the following relationship:

$$K_d(PAR) = m * K_d(490) \quad (2.1)$$

where  $K_d(PAR)$  is the diffuse attenuation coefficient of  $K_d(\lambda)$  integrated over the visible range of the spectrum.

Using the relationship in equation 2.1 they were able to derive  $Z_{eu}$  from remotely sensed data.

The strong linear correlation between  $K_d(PAR)$  and  $K_d(\lambda)$  was discovered by Zaneveld, et al., (1993) in the north-eastern Pacific Ocean. Linear regression equations were reported relating  $\tau_{PAR}(z)$  to  $\tau(490,z)$  in three optical depth ranges in this study. This  $K_d(PAR)/K_d(490)$  correlation was further substantiated by Barnard et al. (1999).

Tang et al. (2007) applied the above-mentioned methods to derive  $Z_{eu}$ . In their findings they concurred that  $K_d$ -derived euphotic depth is more accurate than the chlorophyll based method because euphotic depth depends on all the optically active water constituents, such as SPM, CDOM and chlorophyll. On the other

hand the empirical chlorophyll-based algorithm is most suitable for Case 1 waters where light attenuation is largely a result of phytoplankton pigments.

A numerical model was developed to estimate the vertical distribution of downwelling irradiance based on a look-up table (Liu et al., 2002). They incorporated CDOM absorption, chlorophyll and particle scattering function in their method to account for the optical complexity of Case 2 waters. The shortfall for this model was that it required more accurate information on chlorophyll concentration for it to be used in ocean colour remote sensing. Also, non-algal particles (NAP) were not accounted for in this model. NAP play a crucial role in light attenuation of inland waters. This model was modified further to take into account these suspended sediments and proved to be successful (Liu, 2006).

Mueller and Lange (1989) developed a set of regression models to obtain  $Z_{eu}$  from remote sensing-derived  $K_d(490)$  based on bio-optical provinces within the Northeast Pacific Ocean. However, because the model was developed based on geographic location and specific time of year, it is difficult to apply them in different conditions.

Based on the principle that the vertical variation of subsurface light field is determined by inherent optical properties, (IOP's), Lee et al. (2005b) developed an analytical model to describe the vertical attenuation of downwelling irradiance in the visible spectrum. They showed that  $Z_{eu}$  of PAR region could be estimated from IOP's at wavelength 490nm derived from in-situ and remote sensing data. This method was tested and compared to the chlorophyll-based empirical approach in the south-eastern the China Sea (Chen et al., 2007; Z. Lee et al., 2007).

## **2.2. Attenuation Coefficient**

### **2.2.1. Background**

Defined as the exponential vertical decrease of radiant light field, the vertical downwelling attenuation coefficient  $K_d(\lambda)$  is significant because it quantifies the presence of light in water and the depth of the euphotic depth (Mobley, 2004). It is referred to as an apparent optical property (AOP), because it depends not only on the concentrations of light attenuating components in the water, but also on the angular distribution of the underwater light field which is dependent on solar incidence angle, surface waves and cloud cover. Research has also shown that  $K_d(\lambda)$  is largely determined by the inherent optical properties of the aquatic medium (e.g. absorption coefficient  $a(\lambda)$  and volume scattering function  $b_b(\lambda)$ ) and are not altered significantly by changes in the incident radiation field such as a change in solar elevation (Kirk, 1994). Hence, it is also termed a quasi-inherent optical property.

$K_d(\lambda)$  is strongly correlated with optically active substances in water (suspended sediment, gelstoff and chlorophyll concentration), thus it provides a relationship between biology and optics (A. Morel & Maritorena, 2001a). Also, approximately 90% of the diffusely reflected light from a water body comes from a surface layer of water of depth  $1/K_d(\lambda)$ , hence  $K_d(\lambda)$  is very important for remote sensing. Research has also gone on to show its significance on heat budget studies (Lewis et al., 1990; Manizza et al., 2004; Andre Morel & Antoine, 1994), photosynthesis and primary productivity models, classification of water types and the description of water transparency (Lozano-Rivera, 2009). Euphotic depth is also directly computed from this parameter. It is also an important apparent optical property that provides information on the extinction of downwelling solar irradiance with depth in water.

### 2.2.2. Remote sensing of attenuation coefficient

Various algorithms have been developed to derive the attenuation coefficient from ocean colour remote sensing.

Austin and Petzold (1981) developed an algorithm to derive  $K_d(\lambda)$  from remote sensing data using the band ratio algorithm. They found strong correlations between  $K_d(490)$  and  $K_d$  at other wavelengths. However, this model was not applicable in inland waters. This model has been modified over time to suit the spectral bands of different remote sensing imagery. For instance they modified it in 1986 to retrieve  $K_d(490)$  from the Coastal Zone Colour Scanner, (CZCS) satellite data. Mueller (2000) adapted it to derive  $K_d(490)$  from the Sea Wide Field-of-view Sensor (SeaWiFS) data, whereas Krater et al. (2008) revised it to retrieve  $K_d(490)$  from MERIS data. These algorithms, however focus mainly the derivation of  $K_d(490)$ , instead of the spectral attenuation coefficient.

The other models (Z. Lee et al., 2005a; A Morel & Maritorena, 2001b) that have been developed need intermediate parameters to be computed first to arrive at spectral  $K_d$ . For instance the empirical model by Morel and Maritorena, (2001a) chlorophyll concentration was first derived as an intermediate link, and the method by Lee, et al., (2005a) required that IOP's be derived first to be able to retrieve  $K_d(\lambda)$  from remote sensing data. The disadvantage with them is the introduction of error when parameterising the intermediate factors. Another disadvantage of the methodology by Morel and Maritorena (2001b) is that it is most suitable for case 1 waters, where chlorophyll is the predominant optical property. However for inland lake waters, it would not be accurate.

Table 2-1: An overview of algorithms to derive  $K_d(\lambda)$

METHOD	EQUATION	DESCRIPTION	AUTHOR
Direct one-step Empirical relationship	$K_d(490) = K_w(490) + A[L_w(\lambda_1)/L_w(\lambda_2)]^B$ where: $K_w(490)$ is the diffuse attenuation coefficient of pure water; A and B are coefficients derived from linear regression; $L_w(\lambda_1)$ and $L_w(\lambda_2)$ are water-leaving radiances at wavelengths $\lambda_1$ and $\lambda_2$	Based on the empirical estimation of $K_d(490)$ using the band ratio method. A linear regression was applied to water-leaving radiances or remote sensing reflectances of two bands within the blue-green region ( $\lambda_1=443\text{nm}$ , $\lambda_2=550\text{nm}$ ). $K_d(490)$ is then used to calculate $K_d$ at other wavelengths.	Austin and Petzold (1981)
Two-step Empirical Algorithm with chlorophyll as an Intermediate Link	1. $Chl = 10^{a_0 + a_1\rho + a_2\rho^2 + a_3\rho^3} + a_4$ where: $\rho = \log_{10}(Rrs(490)/Rrs(555)),$ $a_0, a_1, a_2, a_3,$ and $a_4$ are 0.319, -2.336, 0.879, -0.135, and -0.071, respectively, derived statistically from pooled field data that were collected in various parts of the oceans. Then $K_d(\lambda) = K_w(\lambda) + \chi(\lambda)Chl^{e(\lambda)}$ where: $K_w(\lambda), \chi(\lambda)$ and $e(\lambda)$ are derived from statistical analysis of the data	1. Chlorophyll a concentration was first derived from remote sensing reflectance using the OC2v4 empirical algorithm based on blue-green band ratio of Rrs.  2. Chlorophyll a was then used to compute $K_d(\lambda)$ using empirical relationships between the two parameters	O'Reilly, et al. (1998).  Morel and Maritorena, (2001a)

<p>Semi-analytical approach</p>	<p><math>K_d(\lambda) = m_0a(\lambda) + m_1[1 - m_2e^{-m_3a(\lambda)}]b_b(\lambda)</math>          where:  <math>a(\lambda)</math> is the spectral absorption coefficient  <math>b_b(\lambda)</math> is the spectral backscattering coefficient  <math>m_0, m_1, m_2</math> and <math>m_3</math> are coefficients dependent on the water depth and solar zenith angle</p>	<p>Based on the radiative transfer equations developed by Stavn and Weidemann, (1989) where the AOP's are determined by IOP's. <math>a(\lambda)</math> and <math>b_b(\lambda)</math> are first determined using the QAA, then refine the <math>K_d(\lambda)</math> formula of Sathyendranath et al. equation to account for the contribution caused by backscattering coefficient</p>	<p>Lee, et al., (2005a)</p>
---------------------------------	---	---	-----------------------------

## 3. STUDY AREA AND DATASETS

### 3.1. Study area

#### 3.1.1. General Description

Lake Naivasha (Figure 3-1) is a shallow freshwater lake situated at latitude  $0^{\circ}45'$  South, longitude  $36^{\circ}20'$  East with an altitude 1890m above mean sea level. The lake is situated approximately 80km North-West of Nairobi, in the Kenyan Rift valley. Its size fluctuates between 114 and 991km<sup>2</sup>, making it the second largest freshwater lake in Kenya after Lake Victoria. The surface inflow of Malewa, Gilgil and Karati Rivers contribute to the lake water level, with Malewa being the main contributor. It also contributes the highest sediment load from upstream. Karati River is said to disappear underground before reaching the lake. The lake has an average depth of 5m, with the maximum depth of the main lake experienced around the Hippo Point at 7m, whereas the Crescent Island Lake exceeds 20m depth (Harper et al., 1995). The northern part of the lake is the shallowest, making it more susceptible to plant colonisation. Lake Naivasha basin has a total area approximated at 3400km<sup>2</sup>.

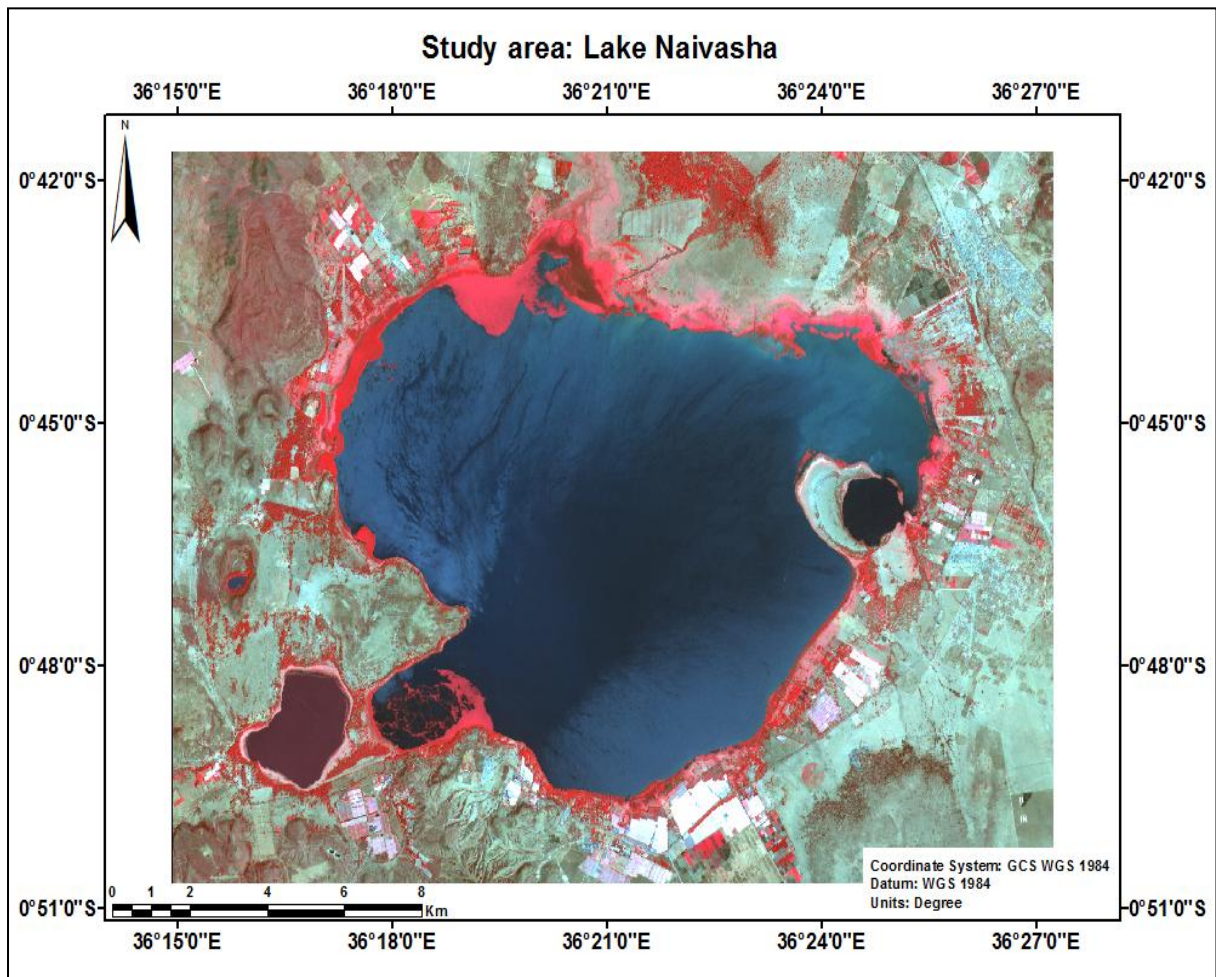


Figure 3-1: Location map of the study area (Source: Aster 2010)

The lake has no surface outlet, and it is believed that the water from the lake seeps into the underlying volcanic rocks and flows southwards and northwards. The lake water freshness is due to a number of factors

including sodium salts extraction by *Cyperus papyrus* and other aquatic plants, underground seepage and subterranean seepage of rainwater from Nyandarua Mountains.

Lake Naivasha boasts of a rich, unique biodiversity, coupled with threats from anthropogenic activities, as such it was declared a wetland of international importance in 1994 under the Ramsar Convention (Jimoh et al., 2007; Odada et al., 2006).

The lake is located in a semi-arid climatic region, with a mean annual precipitation of 600mm. This characteristic is due to Mount Kenya and Nyandarua Range casting a rain shadow over the Lake Naivasha basin when they capture moisture from the monsoon winds. The rainfall distribution has a bimodal pattern with long rains between April and June, and shorter rains in October-November. The annual open water evaporation of the lake is approximately 1700mm, which is said to be higher than the mean rainfall amount. Mean daily temperatures range between 25°C daytime and 9°C at night.

### **3.1.2. Economic significance of Lake Naivasha**

Lake Naivasha is a freshwater lake in an area dominantly arid or semi-arid, making it of immense socio-economic importance to both local and national society. It provides water source for irrigated floriculture and horticulture industries, which provide employment for thousands of local people. The lake supplies water for domestic use for the local community and shares the water table with groundwater aquifers that provide water to Naivasha town and surrounding population. The fishery in the lake has been a source of livelihood for the local community within the lake basin (Harper et al., 2003).

It is a source of water for the drilling of geothermal steam wells and for condensing excess steam during geothermal power generation. Because it supports a vast biodiversity of flora and fauna, the lake is also a tourist attraction with a number of hotels and campsites within its proximity.

Therefore, because of the above-mentioned human activities that take place in and around Lake Naivasha, the lake is under enormous pressure resulting in water pollution and decrease in water levels among other things.

## **3.2. Datasets**

### **3.2.1. Field Data**

#### **3.2.1.1. Data collection**

The in-situ data were acquired during the Lake Naivasha field campaign from 15 September to 06 October 2010. The data included radiometric measurements: water-leaving radiance  $L_w(\lambda)$ , upwelling underwater radiance, downwelling above-water irradiance  $E_d(0^+)$ , and downwelling under-water irradiance at two depths ( $z_0=0.1\text{m}$  and  $z_1=0.6\text{m}$ ); photometric measurements (illuminance and temperature) at various lake depths (0.25m, 0.5m, 0.75m, 1m, 1.25m). Ancillary data also collected were sky and lake conditions, transparency and geographic location of the sampling points.

The sampling sites were selected before each excursion using Google Earth. These were selected based on:

- Location from the main starting point (the Crescent Lake)
- Lake bathymetry to avoid bottom reflectance
- Distance from land to avoid adjacency effect
- Distance between the points chosen based on the spatial resolution of the remote sensing data.

Also the weather conditions, i.e. the cloudiness, and lake conditions, i.e. turbulence (caused by wind speed) were considered during measurements.

Figure 3-2 gives an overview of all the points that were sampled during the fieldwork and the sampling routes that were taken.

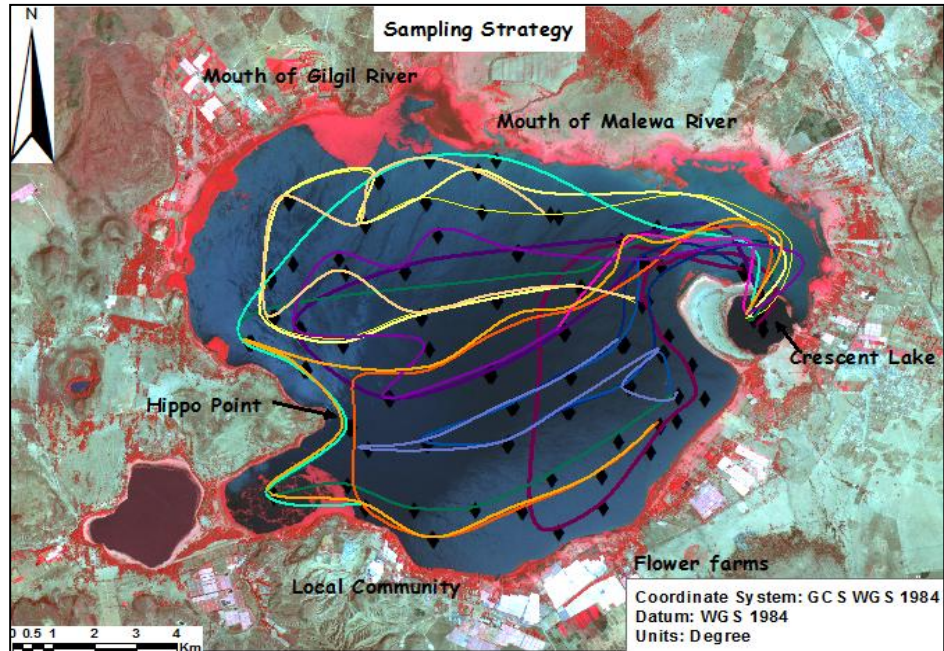


Figure 3-2: Sampling routes during the field campaign

During the days of MERIS satellite overpass, i.e. 17, 20, 23, 26, 29 September, intensive radiometric measurements were done +/- 1 hour the scheduled time. The satellite overpass times were acquired from the European Space Agency during fieldwork planning and preparation stage.

The routes that were used during data collection in the lake are illustrated in Figure 3-2. Sampling the whole lake took four days a time with an average of 10 sampling points a day, totalling 150 sample points at the end of the field campaign.

Table 3.1 gives a summary of the measurements taken on the lake, together with the instruments that were used to complete those tasks.

Table 3-1: An overview of the data collected in the field and equipment used

Measurement	Variable	Instrument
Radiometric	Above-water	TriOs Radiance and Irradiance Sensors
	Water-leaving radiance ( $L_w(\lambda)$ )	
	Above-water downwelling irradiance ( $E_d(0^+;\lambda)$ )	
	Under-water	
	Under-water downwelling irradiance $E_d(0^-;\lambda)$	
Photometric	Underwater light intensity	HOBO Light Intensity Data Loggers
	Temperature	
Ancillary data	Lake state and sky conditions	Photograph camera
	Transparency	Secchi Disk
	Geographic locations of sample points	Garmin 6S GPS
	Date, location description	Physical observations

### 3.2.1.2. Data processing

After the field campaign, the collected data were processed for further analysis. A database was first created in Excel for the data.

The radiometric measurements were first filtered using a number of factors:

- Using the 95% confidence interval to remove the outliers.
- Weather conditions, i.e. the days when it was cloudy, for instance day 13 (29 September 2010)
- The irradiance sensor stopped working on day 11, so the spectralon was used to measure above-water downwelling irradiance, however this meant there was no under-water downwelling irradiance. This meant the measurements after this day could not be used for calculating attenuation coefficient ( $K_d(\lambda)$ ).

### 3.2.2. Satellite Data

#### 3.2.2.1. MERIS Data acquisition

The MEdium Resolution Imaging Spectrometer (MERIS), was used for this study. It is a medium resolution imaging instrument carried on board European Space Agency's Envisat satellite that was launched in 2001. The MERIS was specifically developed for ocean and coastal water research. It has dual spatial resolution of 1200\*1200m, Reduced Resolution (RR) and 300m\*300m, Full Resolution (FR). It operates in the visible and near-infrared spectral range from 390 to 1040nm, with high spectral resolution of between 1.25 and 30nm bandwidth, high radiometric performance, high dynamic range and low sensitivity to polarisation. It was designed with this spectral configuration to make it sensitive to the most important optically active water constituents like CDOM, NAP and chlorophyll pigments (ESA, 2006).

The FR level 1B MERIS imagery was thus selected for this study because of its high spectral and radiometric resolution, and medium spatial resolution that was suitable for the lake size. The data were ordered from European Space Agency (ESA) via their site EOLISA, a free multi-platform interactive tool designed to allow users to access the catalogues of ESA's EO data products, to order them and track their progress.

The images were filtered using the following criteria:

- Image acquisition dates and time had to correspond with date and time of data acquisition, to be used for model validation (i.e. match-up images)
- Cloud coverage of the images since only cloud-free images can be used for the retrieval of water quality parameters

Match-up images are critical in validating models that are developed to derive important parameters from remotely sensed satellite data.

The specifications of this sensor are given below:

Table 3-2: Specifications of MERIS Sensor (courtesy of <http://www.brockmann-consult.de/beam>)

Band no.	Band centre (nm)	Bandwidth (nm)	Solar irradiance ( $E_0$ ) ( $Wm^{-2}nm^{-1}$ )	Application
1	412.5	10	1,713.64	Yellow substance and detrital pigments
2	442.5	10	1,877.44	Chlorophyll and other pigments
3	490	10	1,929.33	Chlorophyll absorption minimum
4	510	10	1,926.84	Suspended sediment
5	560	10	1,800.49	Chlorophyll absorption and fluorescence reference
6	620	10	1,649.71	Suspended sediment
7	665	10	1,530.90	Chlorophyll absorption and fluorescence reference
8	681.25	7.5	1,470.23	Chlorophyll fluorescence peak
9	708.75	10	1,405.47	Fluorescence reference, atmosphere corrections
10	753.75	7.5	1,266.20	Vegetation, cloud, O <sub>2</sub> absorption band reference
11	761.875	2.5	1,249.88	O <sub>2</sub> R- branch absorption band
12	778.75	15	1,175.72	Atmosphere corrections
13	865	20	958.8855	Atmosphere corrections
14	885	10	929.7632	Vegetation, water vapour reference
15	900	10	895.4086	Water vapour

The in-situ data points that were used to perform atmospheric correction and to validate the models are tabulated below:

Table 3-3: MERIS data match-up sites.

Date	Site	Lat	Lon	Time of data collection
20.09.10	S2	S 00°45'37.9	E036°22'23.0	09:55:28
	S3	S 00°45'46.3	E036°21'16.8	10:13:24
	S5	S 00°46'23.9	E036°19'16.5	10:43:38
	S6	S 00°46'01.4	E036°18'22.1	10:58:09
	S8	S 00°44'24.4	E036°18'33.6	11:21:03
	S9	S 00°44'05.7	E036°19'44.4	11:35:53
	S10	S 00°44'42.8	E036°19'33.6	11:46:26
	S11	S 00°44'23.4	E036°20'21.0	11:57:31
23.09.10	S4	S 00°46'23.5	E036°19'15.7	10:57:01
	S6	S 00°45'26.4	E036°18'18.9	11:29:47
	S11	S 00°43'57.7	E036°21'02.5	17:13:56
	Opt1_2	S 00°45'35.4	E036°21'47.2	10:05:34
	Opt3_4	S 00°46'09.5	E036°19'48.8	10:47:40
	Opt4_5	S 00°46'09.1	E036°18'52.0	11:05:06
	Opt5_6	S 00°45'42.3	E036°18'20.2	11:21:28
26.09.10	S2	S 00°46'24.6	E036°22'56.4	10:06:01
	S5	S 00°47'46.6	E036°20'22.3	11:07:48
	S6	S 00°47'47.4	E036°21'26.3	11:24:46
	S9	S 00°46'30.6	E036°23'27.9	11:53:37
	Opt5_6	S 00°47'49.0	E036°20'54.3	11:16:32



## 4. METHODOLOGY

The research aimed at developing an algorithm to derive  $K_d(\lambda)$  from remote sensing data. This was done by first deriving insitu spectral attenuation coefficient from insitu radiometric measurements of underwater irradiance. Then using the  $K_d(\lambda)$ , the spectral euphotic depth was computed. The computed  $R_{rs}(\lambda)$  and  $K_d(\lambda)$  were divided into two datasets, 22 points were used for calibration and the rest for validation of the proposed algorithm. The validated method was then applied to atmospherically corrected MERIS data to retrieve  $K_d(\lambda)$ . Error analysis was done before computing  $Z_{eu}$ , and finally producing map products of  $Z_{eu}$ .

### 4.1. Proposed Approach

Taking into consideration the fact that the methodologies discussed in Section 2.2.2 can only estimate a single spectral value of attenuation coefficient at a time, the proposed approach aimed at estimating the whole spectral range  $K_d$  all at once. This was based on the inverse relationship between attenuation coefficient  $K_d(\lambda)$  and remote sensing reflectance  $R_{rs}(\lambda)$ , incorporated with band ratio approach.

$$K_d(\lambda) = \alpha \left[ \frac{R_{rs}(555)}{R_{rs}(\lambda)} \right]^\beta + \gamma \quad (4.1)$$

where:

$\alpha$ ,  $\beta$  and  $\gamma$  are model coefficients derived using nonlinear regression analysis,  $R_{rs}(555)$  is the reference remote sensing reflectance and  $R_{rs}(\lambda)$  is the spectral remote sensing reflectance.

Error assessment of the between the insitu and modelled datasets was obtained using the mean relative error ( $\epsilon$ ), root mean square error (RMSE) and R-square ( $R^2$ ). These were obtained using equations 4.2 and 4.2. described below:

$$\epsilon = \left( \frac{1}{n} \sum_{i=1}^n \left| \frac{(X^{modelled})_i - (X^{measured})_i}{(X^{measured})_i} \right| \right) * 100\% \quad (4.2)$$

$$RMSE = \left( \frac{1}{n} \sum_{i=1}^n [(X^{modelled})_i - (X^{measured})_i]^2 \right)^{0.5} \quad (4.3)$$

The model was then validated using the remaining part of the insitu  $R_{rs}(\lambda)$ , with the error analysis being performed as well using the above-mentioned methods of statistical analysis. The spectral euphotic depth was subsequently calculated from the modelled  $K_d(\lambda)$ .

#### 4.1.1. Computing $Z_{eu}$ from in-situ measurements

PAR, which defines the spectral range solar radiation from 400 to 700 nm that photosynthetic organisms are able to use in the process of photosynthesis, was first computed by integrating the underwater irradiance at each depth over the visible range (ZhongPing Lee et al., 2005b), that is:

$$PAR(z) = \int_{400}^{700} E_d(\lambda; z) d\lambda \quad (4.4)$$

where  $E_d(\lambda; z)$  is the irradiance to be integrated over the visible spectra at the different depths

$K_d(\text{PAR})$  was then computed from the PAR at the two depths using the method to be discussed below in section 4.1.2.

Based on the linear relationship between  $K_d(490)$  and  $K_d(\text{PAR})$  discussed in Section 2.1, an empirical relationship was first developed between the  $K_d(490)$  and  $K_d(\text{PAR})$ , and  $K_d(620)$  and  $K_d(\text{PAR})$ . The resulting regression equations were used to compute  $Z_{eu}$ . Comparison of the two regression methods was done to get the best method of deriving  $Z_{eu}$  from  $K_d(\lambda)$  product.

From the definition of euphotic depth (Mobley, 2004) where Photosynthetically Active Radiation (PAR) is reduced to 1% of the initial value at the surface, i.e.  $E_d(z_1; \lambda) / E_d(z_0; \lambda) = 0.01$ , where  $z_0=0$  and  $z_1=Z_{eu}$ : Euphotic zone depth is obtained by:

$$Z_{eu} = \frac{4.605}{K_d(\text{PAR})} \quad (4.5)$$

This method was then modified using the regression equation obtained from the  $K_d(490)/K_d(\text{PAR})$  and  $K_d(620)/K_d(\text{PAR})$  correlation, such that  $Z_{eu}$  was retrieved from  $K_d(490)$  and  $K_d(620)$ :

$$Z_{eu} = \frac{4.605}{m * K_d(\lambda) + j} \quad (4.6)$$

where  $m$  and  $j$  are derived by linear regression between  $K_d(\lambda)$  and  $K_d(\text{PAR})$ , and  $\lambda$  represents 490 and 620nm. The  $K_d(\lambda)$ -derived  $Z_{eu}$  was tested for accuracy.

#### 4.1.2. In situ attenuation coefficient

When solar radiation reaches the water surface, about 5% of it is reflected back into the atmosphere and the remainder is transmitted into the water depending on surface roughness. Once it is transmitted into the water, solar radiation interacts with the particulate and dissolved matter present in the water and the water molecules (Mobley, 2004). Hence it is absorbed and/ or scattered by these constituents as it transits down the water column, resulting in it diminishing exponentially with depth ( $z$ ). The rate at which an irradiance field decays as it transits a water column is estimated by the attenuation coefficient ( $K_d(\lambda)$ ) based on the Lambert-Beer law:

$$E_d(z_1; \lambda) = E_d(z_0; \lambda) e^{(-\int_{z_0}^{z_1} K_d(\lambda) dz)} \quad (4.7)$$

where:

$E_d(z_0; \lambda)$  and  $E_d(z_1; \lambda)$  and are spectral underwater irradiance measurements at depths  $z_0$  and  $z_1$ .

Solving for the attenuation coefficient over water depth,  $\Delta z$ , gives:

$$K_d(\lambda) = -\frac{1}{\Delta z} \ln \left[ \frac{E_d(z_1; \lambda)}{E_d(z_0; \lambda)} \right] : |z_1| > |z_0| \quad (4.8)$$

The in-situ radiometric measurements of underwater irradiance ( $z_0$  and  $z_1$  are depths at 0.1m and 0.6m, respectively) were thus used to calculate the  $K_d(\lambda)$  by applying equation 4.8.

#### 4.1.3. Remote sensing reflectance

Remote sensing reflectance ( $R_{rs}(\lambda)$ ) is defined as the ratio of the water-leaving radiance  $L_w(\lambda)$  to the above-surface downwelling irradiance  $E_d(0^+, \lambda)$  (J. L. Mueller et al., 2003a):

$$R_{rs}(\lambda) = \frac{L_w(\lambda)}{E_d(0^+, \lambda)} \quad (4.9)$$

It is a very important apparent optical property that has been used to in estimating optical properties of water through inverse modelling, as well as attenuation coefficient.

Using equation 4.9, the in-situ radiometric measurements of water-leaving radiance and downwelling irradiance were used to compute  $R_{rs}(\lambda)$ . The data was also analysed to be used in the development of  $K_d(\lambda)$  algorithm.

#### 4.1.4. $K_d(\lambda)$ algorithm development

The  $K_d(\lambda)$  was plotted against the inverse of  $R_{rs}(\lambda)$  and their correlation assessed, giving the visuals illustrated in Figure 4.1a to d. The illustrations show a distinct pattern of the relationship between the two parameters, despite different values and times the measurements were taken. Using this correlation, the data was subdivided into 4 distinct classes.

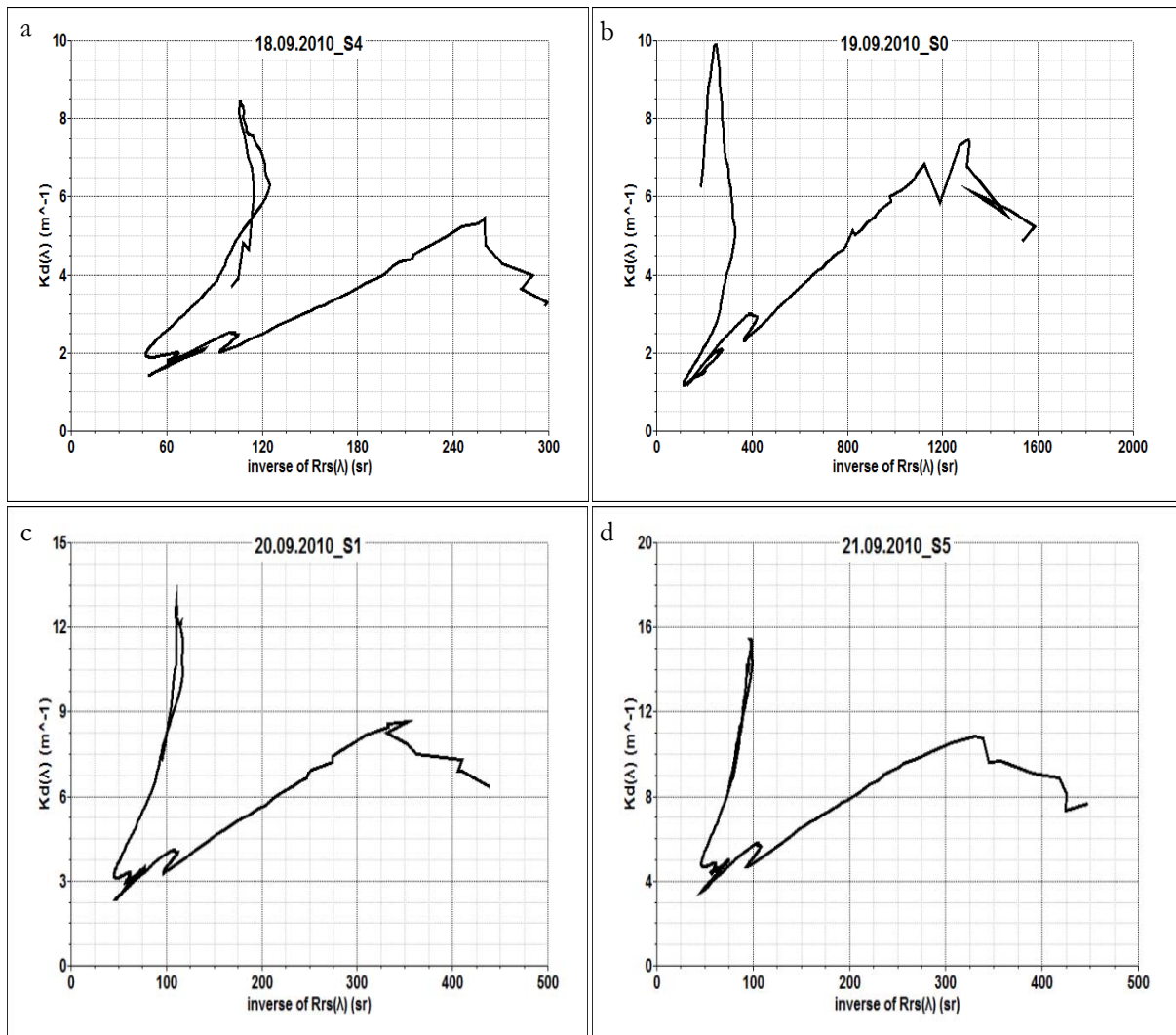


Figure 4-1 a, b, c, d: Relationship between  $K_d(\lambda)$  and  $R_{rs}(\lambda)$

The result of the classification was:

Spectral range 0	320-440nm
Spectral range 1	440-600nm
Spectral range 2	600-800nm
Spectral range 3	800-930nm

Since we are interested in the visible range and PAR the first spectral region (320-440nm) will not be treated in this manuscript.

With the above spectral partitioning, 25% of in-situ  $1/R_{rs}(\lambda)$  and  $K_d(\lambda)$  was employed to develop the numerical algorithm described in equation 4.1 using non-linear regression.

## 4.2. Image Processing

The BEAM and ENVI software were used during image processing. BEAM is an open-source toolbox and development platform for viewing, analysing and processing of remote sensing data that was originally developed for Envisat satellite imagery. ENVI is another used for processing and analysing geospatial imagery.

The MERIS 1B images that were acquired were screened for clouds first, resulting in the image for the 29th of September being discarded. Equation 4.6 (Maseck, 2010) was applied to the MERIS-derived water-leaving radiances to retrieve the water-leaving reflectances.

$$\rho_w(\lambda) = \frac{\pi d^2 L_w(\lambda)}{E_0 \cos(\theta)} \quad (4.10)$$

where:

$\rho_w(\lambda)$  = water-leaving reflectance

$L_w(\lambda)$  = water-leaving radiance recorded at sensor

$E_0$  = Extraterrestrial solar irradiance

$d$  = mean Earth-Sun distance

### 4.2.1. Atmospheric correction

Satellite remote sensing data are modified by the absorption and scattering effects of the atmosphere. These interactions occur as the electromagnetic radiation passes between the Sun and the Earth's surface, and the ground and sensor. This makes the accurate retrieval of inherent optical properties very difficult. Therefore, accurate, practical methods of atmospheric correction must be applied to retrieve the true water-leaving reflectance.

The satellite sensed radiance  $L_t(\lambda)$  or reflectance  $\rho_t(\lambda)$ , is partitioned into several components that correspond to the physical processes:

$$\rho_t(\lambda) = \rho_r(\lambda) + \rho_a(\lambda) + \rho_{ra}(\lambda) + T(\lambda)(\rho_{sfc}(\lambda) + \rho_w(\lambda)) \quad (4.11)$$

where:

the first three terms on the right-hand side of the equation represent the contributions from atmospheric scattering due to air molecules, aerosols, and Rayleigh-aerosol interactions, respectively.  $T(\lambda)$  is the diffuse and direct transmittances of the atmosphere, respectively,  $\rho_{sfc}(\lambda)$  is the effects of surface reflectance (sunglint),  $\rho_{cw}(\lambda)$  reflectance of white caps, and  $\rho_w(\lambda)$  is the water leaving reflectance.

According to Chomko and Gordon (2001),  $\rho_{sfc}(\lambda)$  and  $\rho_{wc}(\lambda)$  have to be avoided and/ or eliminated, thus the equation is left:

$$\rho_t(\lambda) = \rho_{path}(\lambda) + T(\lambda)\rho_w(\lambda) \quad (4.12)$$

where:

$\rho_t(\lambda)$  = top-of-atmosphere reflectance recorded at sensor

$\rho_{path}(\lambda)$  = reflectance from the atmospheric path ( $= \rho_r(\lambda) + \rho_a(\lambda) + \rho_{ra}(\lambda)$ )  
 $T(\lambda)$  = viewing transmittance from the target to the sensor  
 $\rho_w(\lambda)$  = water-leaving reflectance

Atmospheric correction for the match-up data was performed using in-situ measurements of water-leaving reflectance and satellite top-of-atmosphere reflectance based on equation 4.12. MERIS-derived top-of-atmosphere converted to remote sensing reflectances and insitu reflectances measurements were first used to compute the influence contributed by the atmosphere, i.e. the atmospheric path. These were then subtracted from the MERIS top-of-atmosphere reflectances to retrieve water-leaving reflectances from the images.

After converting the image data to water-leaving reflectances, the images were subjected to further processing.

- **Subsetting the images**- it was necessary to reduce the size of the images because they were very large, thus they were affecting the processing time. Only the Lake Naivasha area was clipped out to be used for further processing.
- **Masking out the land**- the land surrounding the lake had to be concealed to make the analysis of the lake water easier. This was done by first building a mask for each image. Band 15 that is band 900nm was chosen for this task because it gives a clear demarcation between land and water. Also, since this is a NIR band, water reflectance is lowest (3-5%), whereas vegetation reflectances are very high. The maximum values for the masked were set at 0.05 and the minimum at 0.
- **Georeferencing the subset image**- this was done to improve the visualisation of the final product of  $Z_{eu}$

#### 4.2.2. Mapping of euphotic depth

The validated  $K_d(\lambda)$  model was applied to MERIS products of water-leaving reflectance, and accuracy assessment done using  $\epsilon$ , RMSE and  $R^2$ .

The empirical methods that were developed to derive  $Z_{eu}$  from  $K_d(490)$  and  $K_d(620)$  were applied on the  $K_d(490)$  and  $K_d(620)$  MERIS products to derive  $Z_{eu}$  using ENVI software and the best method of the two defined. The method was finally used for mapping  $Z_{eu}$  and the spatial analysis of light penetration in the lake was done. The final product was



## 5. RESULTS

This chapter details the main findings of this research. The results of the derived spectral  $K_d$  and spectral radiation penetration depth are illustrated below, together with remote sensing reflectance ( $R_{rs}(\lambda)$ ) results that were computed from in-situ radiometric measurements of downwelling irradiance,  $E_d(\lambda)$ , and water-leaving radiance,  $L_w(\lambda)$ . In-situ spectral  $Z_{eu}$  results are also demonstrated here, together with the PAR and empirically-derived  $Z_{eu}$ . The developed  $K_d(\lambda)$  model that is based on defined spectral classes is demonstrated as well. At each stage the developed methods were evaluated for accuracy against in-situ measurements, and the findings thereof highlighted below. The validated  $K_d(\lambda)$  and  $Z_{eu}$  models were further substantiated using the atmospherically corrected  $R_{rs}(\lambda)$  products of MERIS match-up data. The good correlation results between the modelled MERIS products of  $K_d(\lambda)$  and  $Z_{eu}$  in-situ measurements are also demonstrated in this chapter. The final  $Z_{eu}$  map products are shown and used for the spatial analysis of  $Z_{eu}$  in Lake Naivasha.

### 5.1. In-situ Euphotic depth

The in-situ radiometric measurements of underwater downwelling irradiance ( $z_0$  and  $z_1$  depths at 0.1m and 0.6m, respectively) were used to calculate the spectral attenuation coefficient ( $K_d(\lambda)$ ). Photosynthetically Active Radiation (PAR) from each depth were also derived from underwater irradiance measurements, then  $K_d(\text{PAR})$  and thus  $Z_{eu}$  were then computed as described in Section 4.1.1. The results of spectral  $K_d$  and depth of light penetration are shown in Figure 5-1a and b.

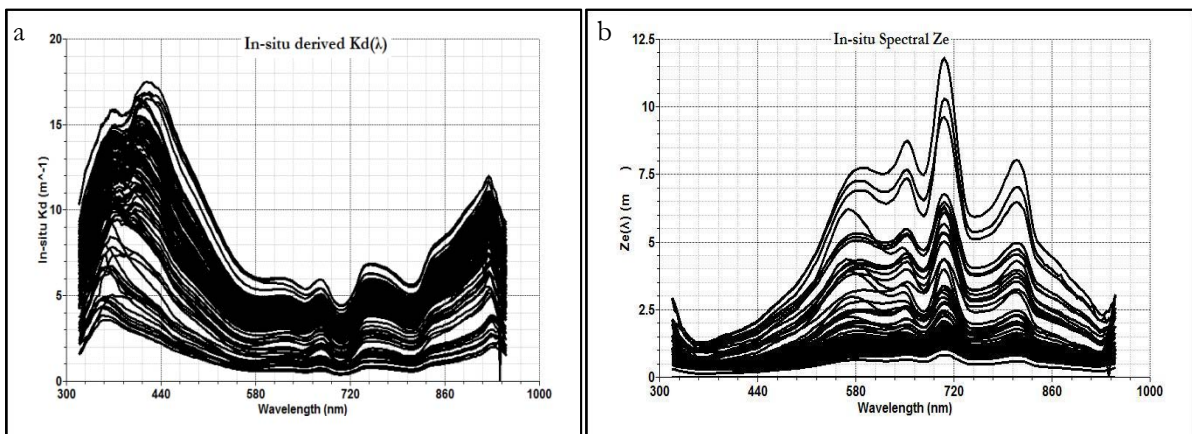


Figure 5-1a, b: Spectral  $K_d$  and depth of light penetration

The spectral diffuse attenuation coefficients and depth ranges between 0.5-17.5m<sup>-1</sup> and 0.2-11m respectively. There is a significant trough in  $K_d$  at 705nm that is proportional to the peak in  $Z_{eu}$  at the same wavelength. This was due to the fluorescence of chlorophyll pigments in that wavelength.

The inverse relationship (equation 4.5) between the in-situ  $K_d(\text{PAR})$  and  $Z_{eu}$  is shown in Figure 5-2 below.

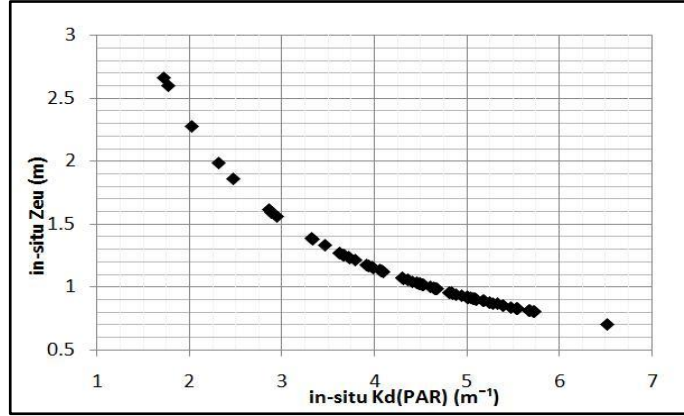


Figure 5-2: Relationship between in-situ derived  $K_d(\text{PAR})$  and  $Z_{eu}$

To develop the local model for estimating  $Z_{eu}$  from spectral attenuation coefficient  $K_d(\text{PAR})$  was plotted against both  $K_d(490)$  and  $K_d(620)$ . Kratzer et al. (2003), however only highlighted the relationship between  $K_d(\text{PAR})$  and  $K_d(490)$ . The outcome is highlighted in Figure 5-3.

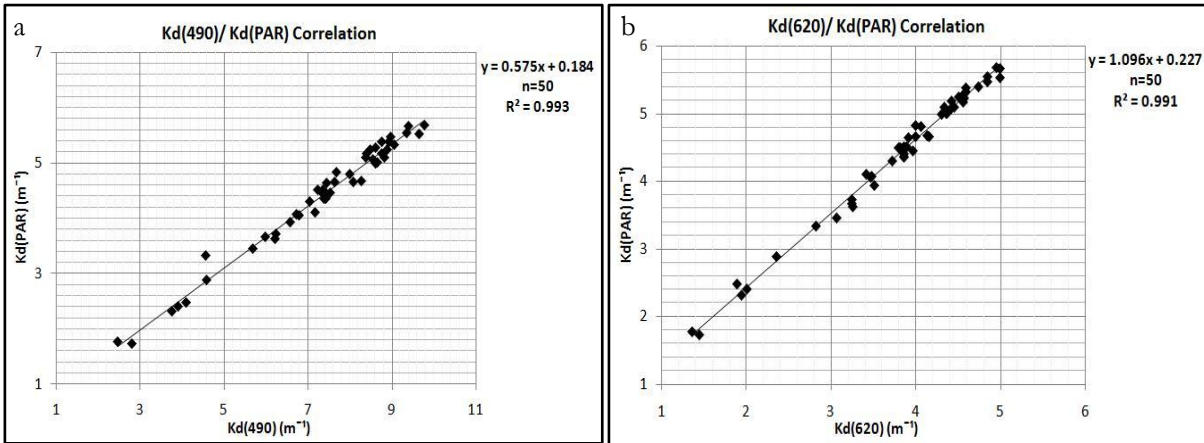


Figure 5-3 a, b: Comparison of  $K_d(\text{PAR})$  and  $K_d(490)$ ;  $K_d(\text{PAR})$  and  $K_d(620)$

The regression analysis generated the following relationship:

$$K_d(\text{PAR}) = 0.575 * K_d(490) + 0.184 \quad (5.1)$$

$$K_d(\text{PAR}) = 1.096 * K_d(620) + 0.227 \quad (5.2)$$

Replacing  $K_d(\text{PAR})$  from equation 4.5,  $Z_{eu}$  was derived empirically from both  $K_d(490)$  and  $K_d(620)$  by:

$$Z_{eu} = \frac{4.605}{0.575 * K_d(490) + 0.184} \quad (5.3)$$

$$Z_{eu} = \frac{4.605}{1.096 * K_d(620) + 0.227} \quad (5.4)$$

respectively.

From the regression, it can be seen that the gradient for  $K_d(\text{PAR})$  against  $K_d(620)$  is closest to 1, as compared to that of  $K_d(490)$  that is just above 0.5.

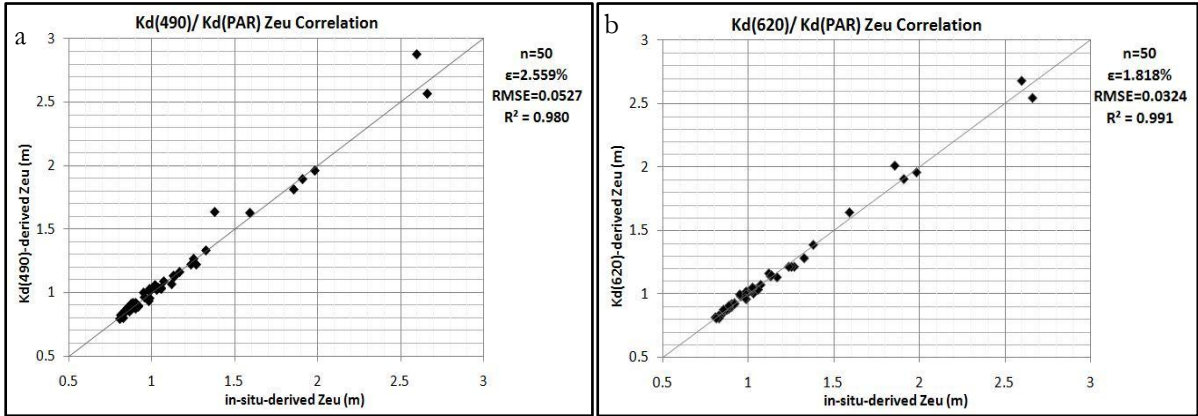


Figure 5-4 a, b: Comparison of  $K_d(\text{PAR})$ -derived to  $K_d(490)$ -derived  $Z_{eu}$  and  $K_d(620)$ -derived  $Z_{eu}$

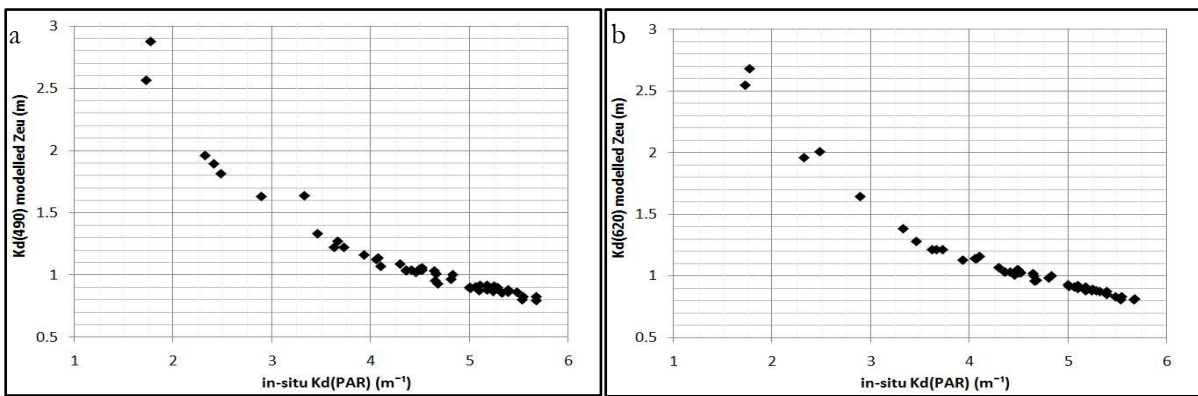


Figure 5-5 a, b: Correlation of modelled  $Z_{eu}$  to in-situ  $K_d(\text{PAR})$

The empirical  $K_d(490)$  and  $K_d(620)$  methods of deriving  $Z_{eu}$  both gave very high results as indicated by the high correlation of  $R^2 > 0.98$ , very low mean relative error 2.56 and 1.83%, and RMSE 0.05 and  $0.03\text{m}^{-1}$  respectively. However, results show that the  $K_d(620)$  model produced higher accuracy. The modelled  $Z_{eu}$  were also plotted against in-situ  $K_d(\text{PAR})$  to analyse if they produce the expected exponential correlation. The outcome in Figure 5-5 illustrate excellent correlation when compared to the original data in Figure 5-2.

## 5.2. Attenuation coefficient model calibration and validation

To derive the  $K_d(\lambda)$  model coefficients the spectra were partitioned to different spectral ranges determined by the relationship between the field-derived inverse of  $R_{rs}(\lambda)$  and  $K_d(\lambda)$ . Non-linear regression analysis was applied to part of the data to calibrate the algorithm, and part was used for validation. Because of the large datasets, the average values of RMSE,  $\epsilon$  and  $R^2$  are given.

The results for the model calibration and validation from field measurements are highlighted below:

Table 5-1: Accuracy Assessment of  $K_d(\lambda)$  models

Spectral Range				Calibration		Validation		
	$\alpha$	$\beta$	$\gamma$	RMSE	$R^2$	RMSE	$\epsilon$ (%)	$R^2$
440-600	3.752	1.245	-0.16	0.275	0.974	2.805	23.436	0.976
600-800	1.92	0.737	1.079	0.115	0.77	0.82	32.031	0.797
800-930	1.846	0.803	0.01	0.078	0.925	0.262	17.698	0.98

The following equations were thus applied to the validation dataset:

$$440-600 \quad K_d(\lambda) = 3.752 * [R_{rs}(555)/R_{rs}(\lambda)]^{1.245} - 0.16$$

$$600-800 \quad K_d(\lambda) = 1.92 * [R_{rs}(555)/R_{rs}(\lambda)]^{0.737} + 1.079$$

$$800-930 \quad K_d(\lambda) = 1.846 * [R_{rs}(555)/R_{rs}(\lambda)]^{0.08} + 0.01$$

The results were also plotted to illustrate the correlation of the developed model to the in-situ data.

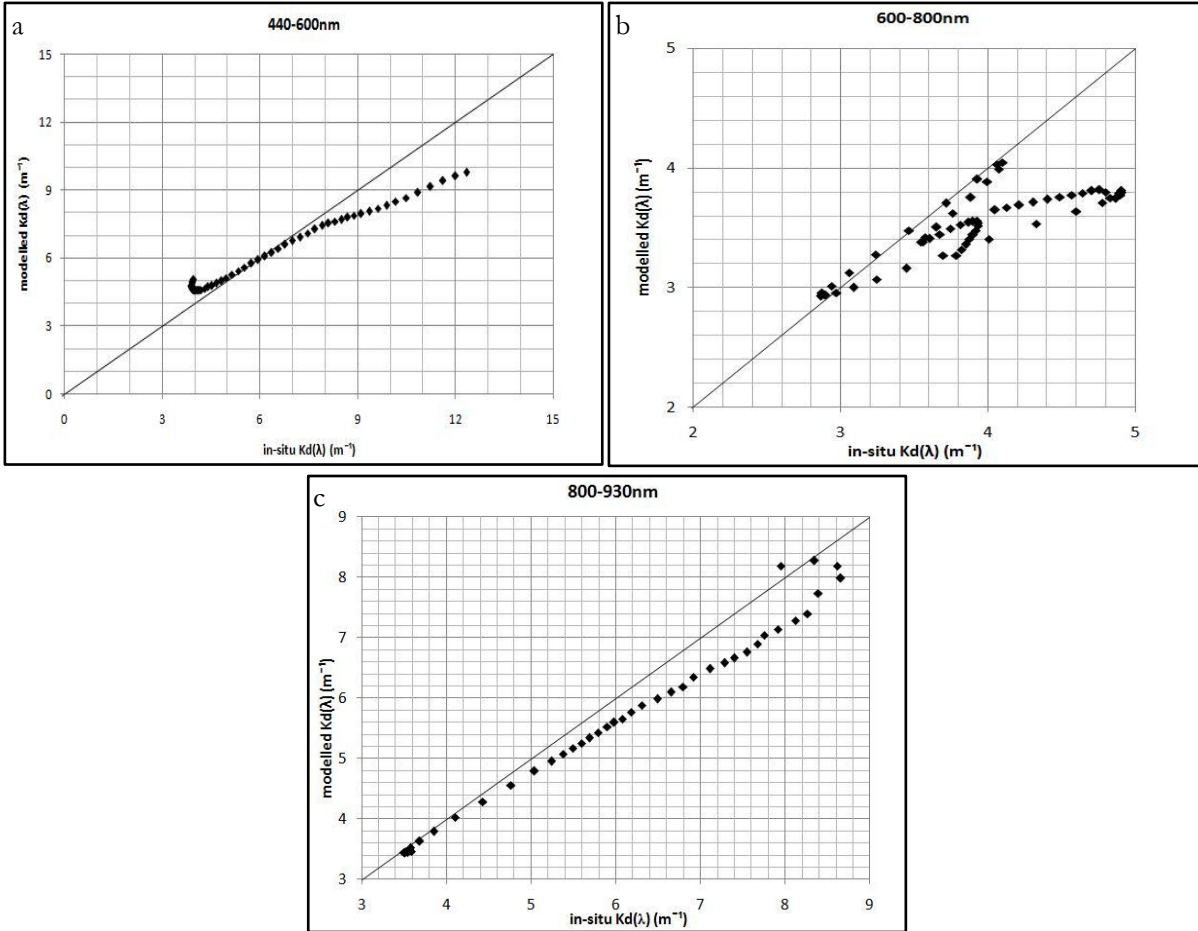


Figure 5-6 a, b, c: Comparison between in-situ  $K_d(\lambda)$  and modelled  $K_d(\lambda)$  based on the spectral regions

### 5.3. Model testing using MERIS match-up data

#### 5.3.1. Atmospheric Correction

Atmospheric correction is performed to remove any influence caused by the atmosphere on the water-leaving reflectance. The AC algorithm was applied to the Match-up images, and substantiation done with in-situ-derived remote sensing reflectance. The correlation between the in-situ and MERIS-derived  $R_{rs}(\lambda)$  is highlighted in terms of the statistical analysis in Table 5-2 and graphical presentation in Figure 5-7a to d. The atmospheric correction was generally successful in all the MERIS match-up data, as depicted by the high correlation that resulted, i.e.  $R^2 > 0.90$ . The RMSE for all the images is  $> 0.002sr^{-1}$ . The 17<sup>th</sup> and 26<sup>th</sup>, however gave high relative error compared to the other days.

Table 5-2: Statistical analysis of the atmospheric correction of MERIS match-up data

Date	RMSE ( $\text{sr}^{-1}$ )	$\epsilon$ (%)	$R^2$
17/09/2010_S8	0.00132	20.561	0.93
20/09/2010_S11	0.00153	10.039	0.934
23/09/2010_Opt3_4	0.00199	26.548	0.968
26/09/2010_S9	0.00187	19.952	0.964

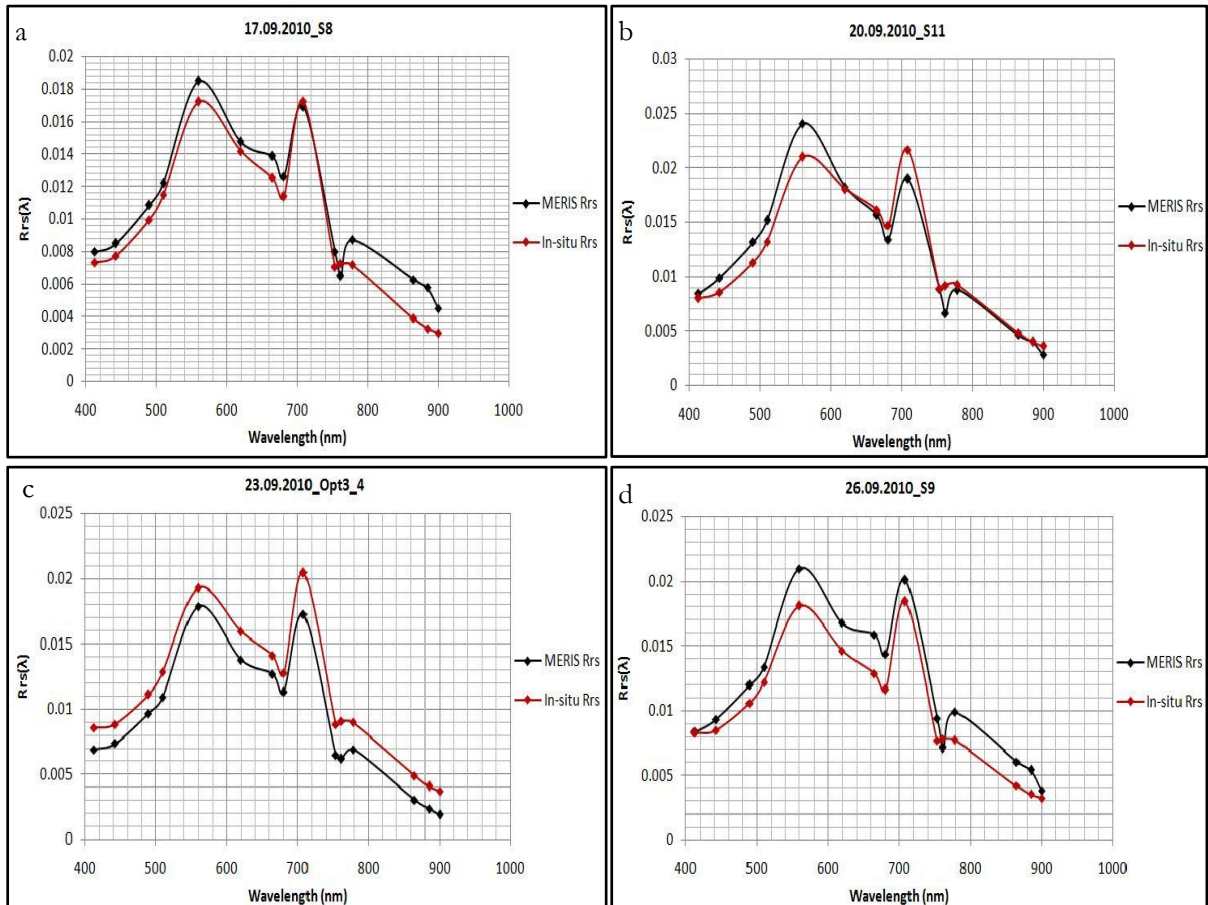


Figure 5-7.3a, b, c, d: Accuracy assessment of atmospheric correction

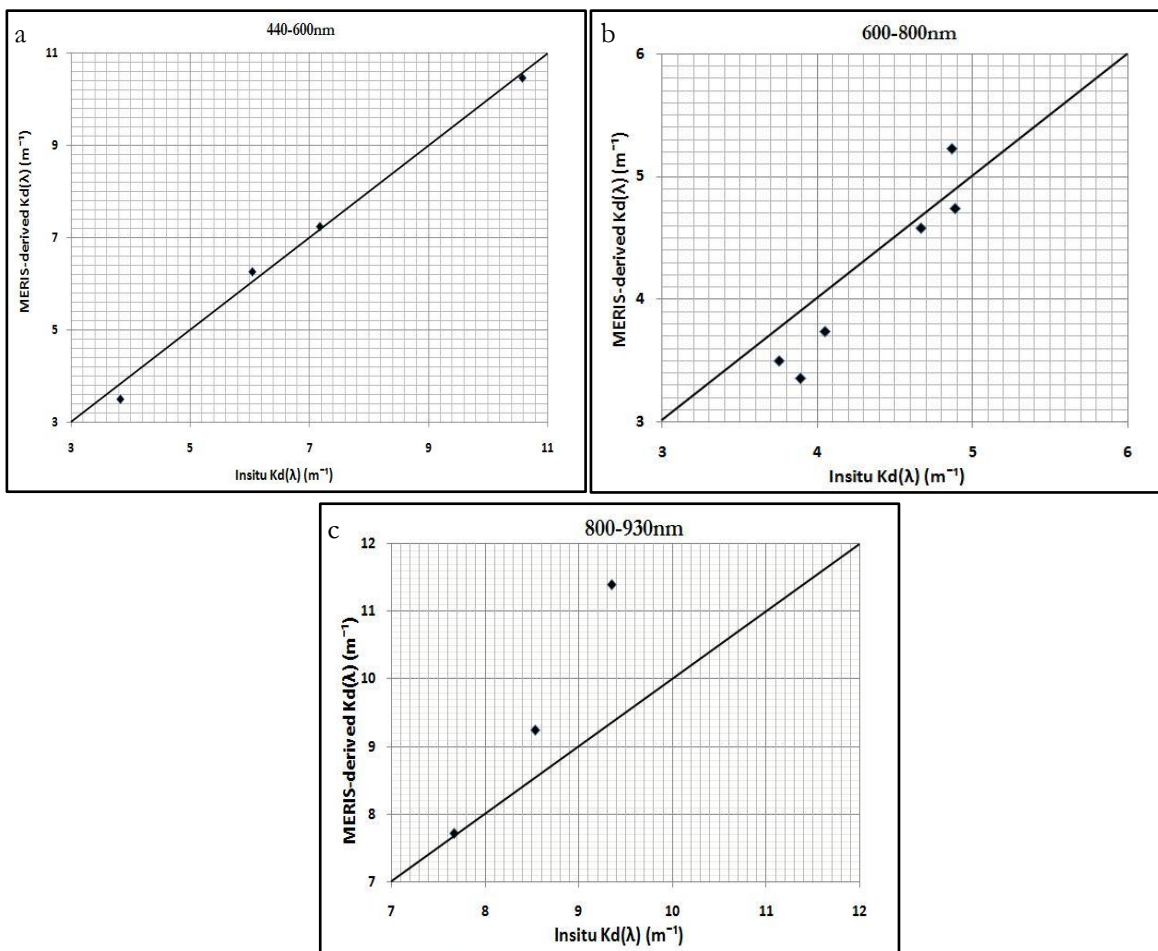
### 5.3.2. Model Validation with MERIS

The developed  $K_d(\lambda)$  model was applied to the atmospherically corrected and validated  $R_{rs}$  product of MERIS match-up data to retrieve  $K_d(\lambda)$ . However, since MERIS does not have band 555, band 560nm was used in the model. Error analysis was performed using RMSE and  $R^2$  by selecting sample points from field data matching with  $\pm 1$  hour the image was taken and comparing with the  $K_d(\lambda)$  derived from the satellite data.

Table 5-3: Error analysis of  $K_d(\lambda)$  model on MERIS data

		MERIS Match-up Data			
	Time of acquisition	17/09/2010	20/09/2010	23/09/2010	26/09/2010
440-600	RMSE	1.452	0.819	1	0.767
	R <sup>2</sup>	0.979	0.996	0.985	0.983
600-800	RMSE	1.334	0.336	0.204	0.216
	R <sup>2</sup>	0.782	0.767	0.841	0.742
800-930	RMSE	2.8	3.726	2.03	1.883
	R <sup>2</sup>	0.931	0.936	0.932	0.933

The results show that  $K_d(\lambda)$  derived on MERIS moderately accurate, with the lowest accuracy being spectral range 3 because it gave the highest RMSE values on the match-up days. Figure 5-8 also illustrates that 800-900nm is least accurate.


 Figure 5-8 a, b, c: Graphical comparison of the  $K_d(\lambda)$  models on MERIS data to measured  $K_d(\lambda)$ 

### 5.3.3. Mapping euphotic depth

$Z_{eu}$  was first computed from the MERIS products of  $K_d(\lambda)$  using the regression models developed ( $K_d(490)$  and  $K_d(620)$  empirical models) in section 5.2. The match-up points used during the validation

process are shown in Table 3-3. The results of the analysis are presented in Figure 5-9, pointing out that the  $K_d(620)$  model was more accurate the commonly used  $K_d(490)$  model.

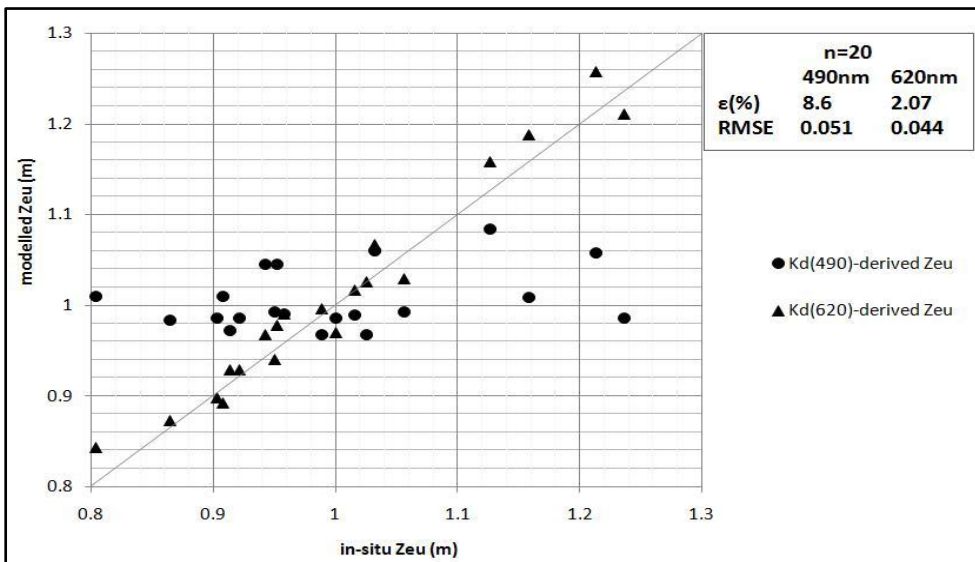


Figure 5-9: Comparison of MERIS  $Z_{eu}$  products derived from  $K_d(490)$  and  $K_d(620)$

The spatial profiles, that is North-to-South and West-to-East, of euphotic depth in the lake are shown in Figure 5-10. Their position is further highlighted on the maps in Figure 5-11. A general trend in  $Z_{eu}$  in all the images is highlighted by the spatial profiles. The  $Z_{eu}$  ranges between 0.9 and 1.13m in the main part of the lake. High  $Z_{eu}$  is experienced in the northern part of the lake and the southern part. There are also spikes in the  $Z_{eu}$  product of 23/09/2010.

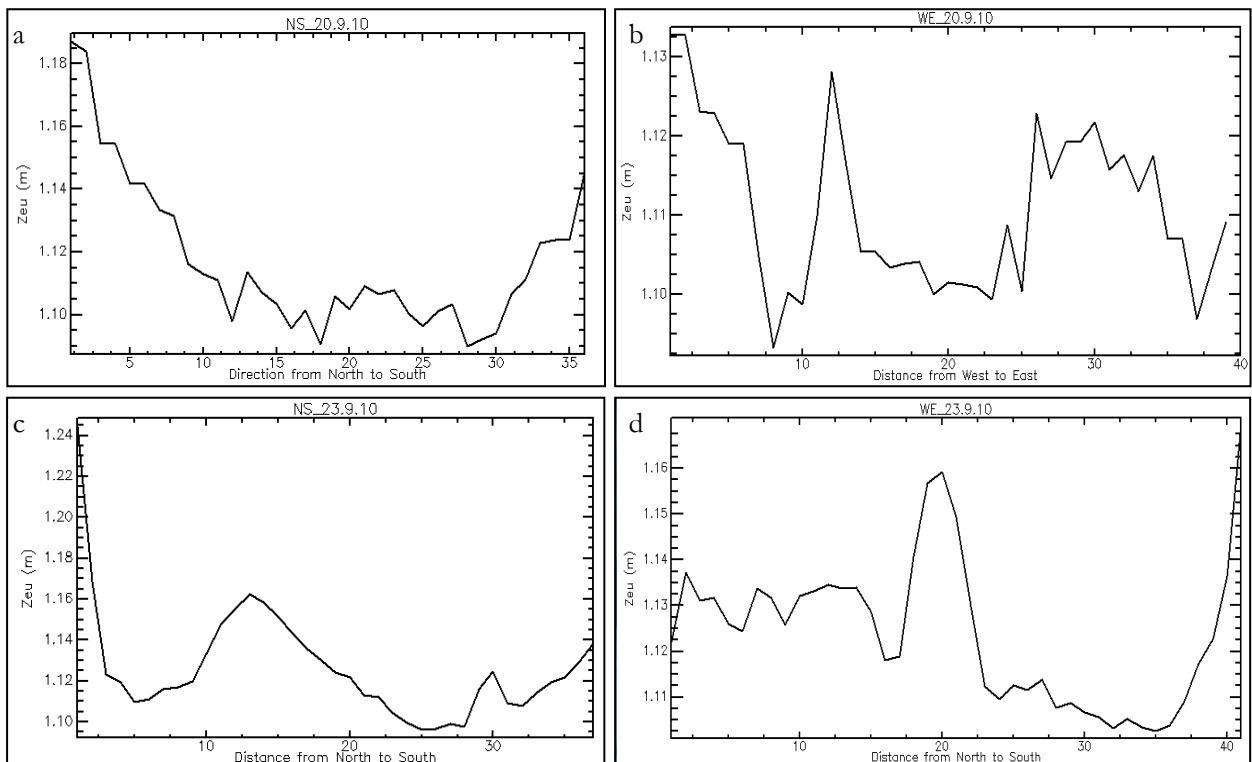


Figure 5-10a, b, c, d: Spatial profile of  $Z_{eu}$  in the lake- a and c North-South profiles, b and d West-East profiles

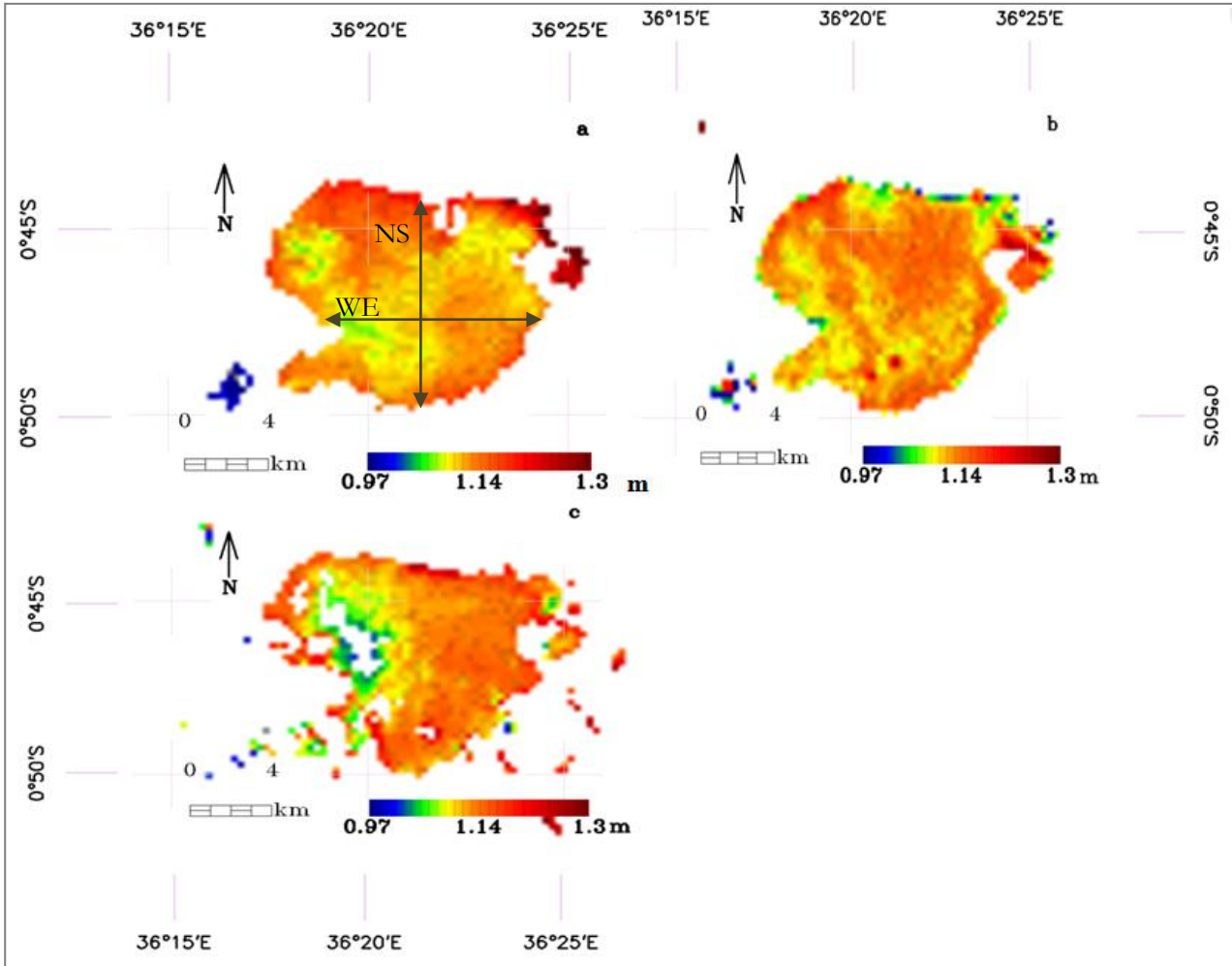


Figure 5-11 a, b, c: Maps showing spatial variation showing spatial variation of Zeu over 7 days (a-20.09.10; b-23.09.10; c-26.09.10 products), the NS and WE cross-sections are shown in full lines.

## 6. DISCUSSION

The study revealed an approach of deriving  $K_d(\lambda)$  from  $R_{rs}(\lambda)$  measurements. A local algorithm was also built to retrieve  $Z_{eu}$  from  $K_d(620)$ . The study illustrated that there is a distinct relationship between the  $K_d(\lambda)$  and the inverse of  $R_{rs}(\lambda)$  that could be distinctly classified into 3 spectral classes. This chapter will discuss in detail the major findings of the research and the limitations thereof.

### 6.1. Field Data

Intensive radiometric data collection was done in Lake Naivasha for this research. On the MERIS satellite overpass days, the measurements were increased to improve the atmospheric correction methodology as well as for validating the developed  $K_d(\lambda)$  model.

Radiometric measurements were taken every day between 0900 hours and 1200 hours, under clear skies, wind speed  $5\text{ms}^{-1}$ , among other sampling strategies. This was in line with the recommended radiometric measurement times as given in the radiometric measurements and data analysis protocols (J. L. Mueller et al., 2003a), which states that the measured radiance should be coming from the water surface between  $30^\circ$  and  $50^\circ$  solar zenith angle. However, the cloudy conditions, together with rainfall and strong winds greatly affected the field campaign. The issue of surface reflectance thus had to be taken into consideration. When the water surface is smooth almost all the radiation is reflected away in a single direction, causing sun glint. Water surface roughness is mainly affected by wind speed and illumination viewing geometry. Calm seas reflect less than rough seas for small-look angles but as look angle increases, calm seas reflect more than rough seas.

Another issue of particular interest was the frequency of the strong currents and rains that are frequently experienced in the lake, especially in the afternoons. These result in the upwelling, and that ultimately leading to the bottom water bringing some nutrients to the surface. The nutrients fertilise phytoplankton in the mixed layer, which are eaten by zooplankton, and these are in turn eaten by small fish (Microbiologyprocedure.com). Although these winds contribute to error during measurements they play a crucial role in contributing to the continuation of whole ecosystem of the lake. The lake was therefore termed Nai'posha by the local community because it is a highly dynamic lake, experiencing frequent storms.

Another factor that affected data collection was the breakdown of the irradiance sensor on day 10 of our campaign. This ultimately meant no underwater downwelling irradiance measurements would be taken, although the spectralon was used to measure downwelling above-water irradiance.

#### 6.1.1. Spectral Reflectance signature of Lake Naivasha water

Lake Naivasha spectral reflectance shape exhibits that of case 2 waters. Three optically active components affect the characteristics found in the spectral reflectance curve of freshwater: chlorophyll pigments, NAP, and CDOM. Previous studies have identified the sources of the characteristics highlighted in Figure 5-1.

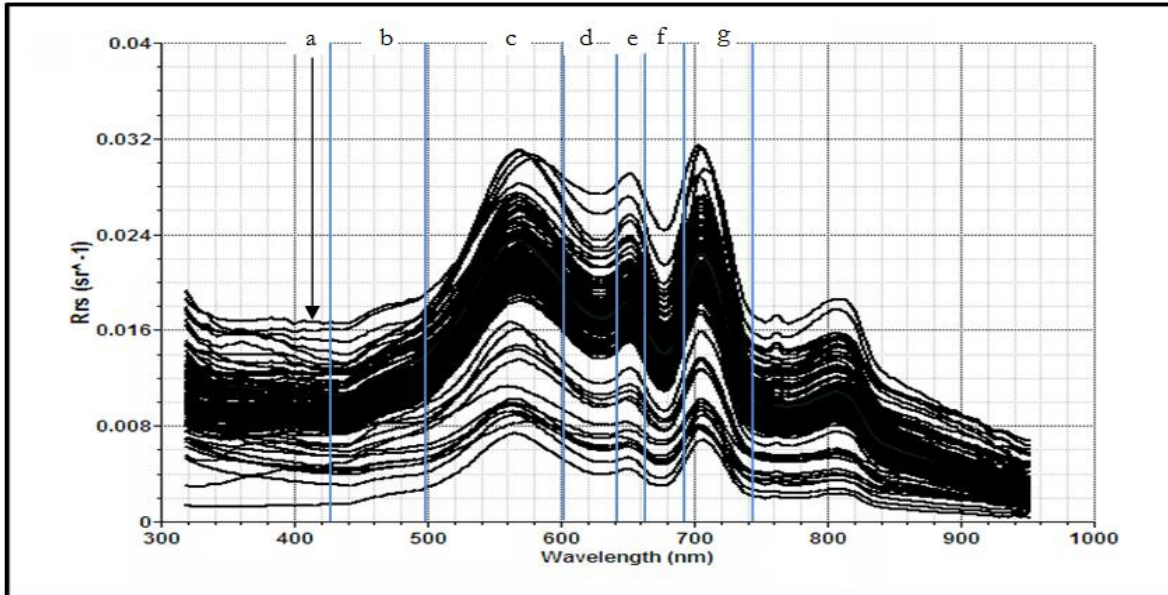


Figure 6-1: Spectral signature of the lake water

The first feature at approximately 440 nm is attributed to absorption by chlorophyll, dissolved organic matter and suspended sediment (A. A. Gitelson et al., 1999). The absorption feature between 450 and 525 nm (b) is attributed to the presence of yellow and red pigments (Holtz & Tanya, 2007). The spectral range 550-600 nm (c) contains the green peak, which is attributable to minimal absorption by phytoplankton pigments and, thus, maximum scattering by algal cells (A. Gitelson, 1992; Holtz & Tanya, 2007). The subsequent trough within the 620- 630 nm range (d), is the result of absorption by phycocyanin. The small reflectance peak at approximately 650nm (e) is attributed to backscattering from CDOM (A. Gitelson, 1992). This attribute is also known to be affected by phycocyanin concentration because it is the location where phycocyanin fluorescence emission is maximum. The trough feature at approximately 675 nm is the chlorophyll a absorption maximum (f) (Holtz & Tanya, 2007). However, reflectance here depends mainly on the non-organic suspended matter present in water. The reflectance peak in the near infrared section of the spectrum, that is within the range of 698 and 712 nm (g), is the result of scattering from algal cells, the pigment and water combined, and particulate matter. However, the location and height of this peak also results from chlorophyll a concentration. Peak shifts toward longer wavelengths and increase in height are signals of increased chlorophyll a concentration (Han & Rundquist, 1997). Reflectance at wavelengths longer than 750nm are attributed to organic and non-organic suspended matter concentrations (Han, 1997).

### 6.1.2. Euphotic Depth from in-situ measurements

Because depth of light penetration cannot be measured directly from the water, it was determined straight from  $K_d(\lambda)$ . The results of both  $K_d(\lambda)$  and spectral euphotic depth are shown in Figure 5-1a and b.  $K_d$  varies with wavelength because it is a function of the IOP's, i.e. absorption and backscattering coefficients; it takes the profile of the bulk absorption coefficient against wavelength (Mobley, 2004). When light is attenuated by these water constituents,  $K_d(\lambda)$  increases and the  $Z_{eu}$  decreases. The total particulate absorption is high in the blue region because of the combined light absorption by phytoplankton, NAP, CDOM and water molecules, resulting in high  $K_d(\lambda)$  in this spectral region. Between the blue and the green region attenuation of light decreases as absorption decreases, resulting in  $Z_{eu}$  rising. This is because of the decrease of the absorption coefficient by chlorophyll pigments, NAP and CDOM. The low  $K_d$  between 550 and 650nm is a result of the diminished absorption coefficient of the water constituents. In

the red part of the spectrum, attenuation due to dissolved materials is negligible, so that attenuation in the red is due primarily to particles. The small peak of  $K_d$  around 665nm is due to the absorption by chlorophyll pigments again. The attenuation coefficient in the red is an excellent proxy for the total volume of particles. Light penetration is highest around 705nm, where there is a dip in  $K_d(\lambda)$ . The rationale for this peak chlorophyll fluorescence. Chlorophyll pigments, after absorbing light in the blue part of the spectrum, will release it in the red region, a process called fluorescence. The higher the peak, the higher the concentration of phytoplankton in the water body. Randolph (2007) evaluated algorithms that are based on chlorophyll fluorescence in his work.

The relationship between  $K_d(\lambda)$  and IOP's has long been under study. For instance the Monte Carlo simulation of the radiative transfer equation has been used over time to estimate particularly diffuse attenuation coefficient, to the IOP's (Kirk, 1994). Loisel and Stramski (2000) also developed a model that links  $K_d$ , IOP's and subsurface reflectance in the upper ocean based on the radiative transfer theory. A comparison is illustrated between absorption coefficients from literature and the in-situ measurements of  $K_d(\lambda)$  below:

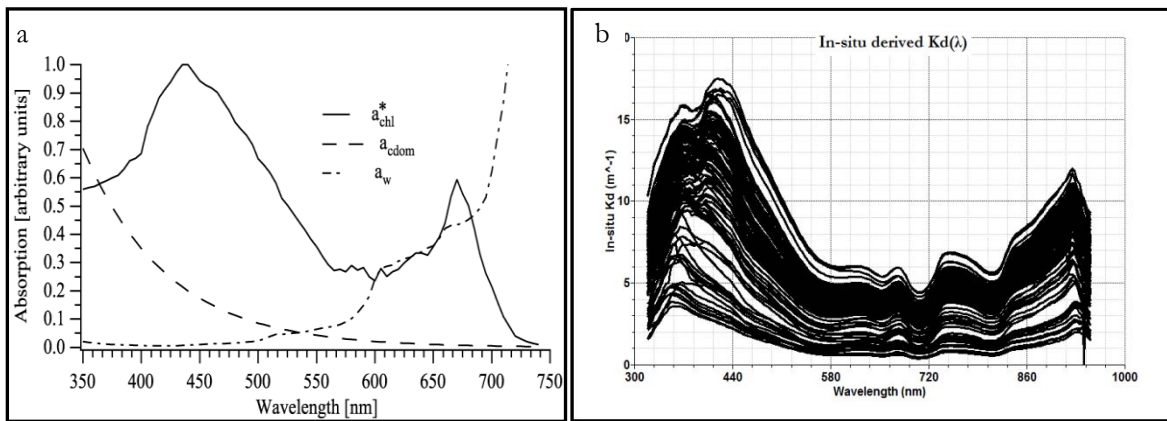


Figure 6-2a, b: the comparison of the general spectral trend between  $a(\lambda)$  and  $K_d(\lambda)$ - (Figure a taken from Mueller, et al., (2003b))

The relationship between the absorption coefficient and  $K_d(\lambda)$  can be identified from the similarity of the general trend between the two graphs.

$Z_{eu}$  in the lake varied between 0.9-1.3m, with the high  $Z_{eu}$  experienced at the Crescent Island Lake. This is because the water in this part of Lake Naivasha is clearer, with Secchi depth ranging around 0.7m, whereas the Secchi depth in the main lake is The results concur with other studies that have been done on euphotic depth of shallow lakes. For instance studies done by Zhang et al. (2006) reveal that the  $Z_{eu}$  of Lake Taihu, which is defined as a typical shallow lake, ranges between from 1.04 to 1.95m. They are with the results measured by Philips et al. (1995) in Okeechobee Lake, a large shallow lake, in Florida, United States of America.

The empirical model that was developed to derive  $Z_{eu}$  from  $K_d(620)$  was successful. The Although research has shown that 490nm is the best in estimating PAR because this is the wavelength near the maximum wavelength penetration in clear natural waters and the fact that it is often used in remote sensing observation, the results show that the local 620nm model was more accurate in predicting  $Z_{eu}$ . This is indicated by higher  $R^2 > 0.99$ , lower RMSE of 0.0324m and  $\epsilon$  of 1.82%.

## 6.2. $K_d(\lambda)$ Model Calibration and Validation

Previous studies have described the relationship between a single wavelength of  $K_d$  and other parameters (Table 2-1). This research, however has gone a step further by first describing the correlation between  $R_{rs}(\lambda)$  and  $K_d(\lambda)$ . Both  $R_{rs}(\lambda)$  and  $K_d(\lambda)$  are AOP's can be obtained from IOP's, however they exhibit inverse correlation. This is illustrated by Figure 6-2.

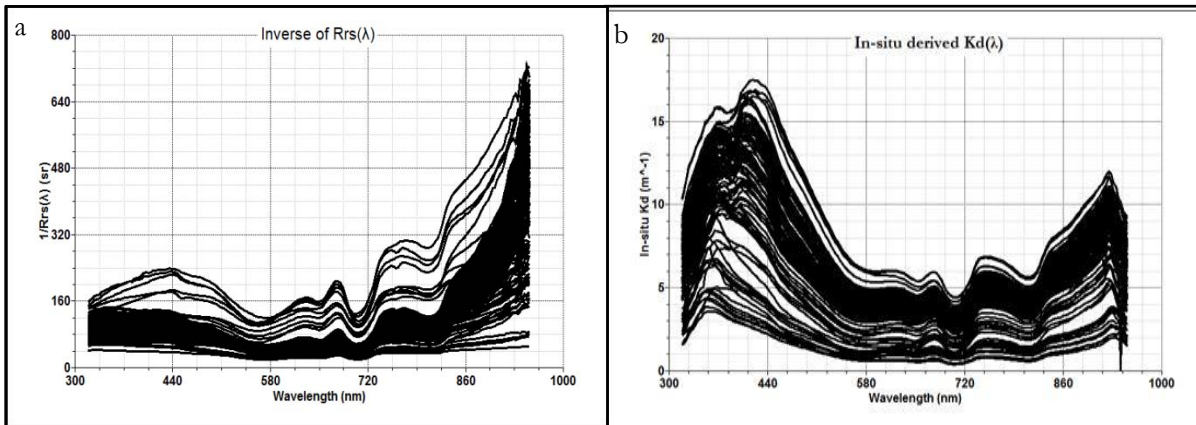


Figure 6-3 a, b: In-situ derived  $R_{rs}(\lambda)$  and  $K_d(\lambda)$

The first spectral range, which is 440-600 nm is a result of absorption by chlorophyll pigments, dissolved organic matter and suspended sediment in the water. Absorption by the water constituents decreases within this range, resulting in the attenuation coefficient diminishing. However  $R_{rs}(\lambda)$  in this range increases as the absorption by water constituents diminish. Between 600 and 800nm, spectral class 2, the outlines of both  $R_{rs}(\lambda)$  and  $K_d(\lambda)$  are undulating due to the absorption and scattering caused by the various water constituents. The scattering of light between 550 and 600nm result in high  $R_{rs}(\lambda)$ . Attenuation is low here because it is only caused by scattering; absorption is minimal. In the 800-930nm spectral range reflectance is a result of scattering of organic and non-organic suspended matter concentrations only, and decreases across the longer wavelengths.  $K_d(\lambda)$ , on the other hand rises steadily. Therefore, the  $K_d(\lambda)$  model was developed based on this inverse relationship between the two parameters.

Field data was divided into two datasets, one set for model development and the other for substantiating the developed model. The proposed  $K_d(\lambda)$  method was based on the correlation between the inverse of  $R_{rs}(\lambda)$  and  $K_d(\lambda)$ . The in-situ  $1/R_{rs}(\lambda)$  and  $K_d(\lambda)$  data were selected at random and plotted against and these revealed distinct delineations, as shown in Figure 4-1a to d. Based on these demarcations, the spectra being partitioned into 4 distinct classes, i.e. 400-440nm, 440-600nm, 600-800nm and 800-930nm. For each spectral range model coefficients were defined based on equation 4.1. The results in Table 5-1 show that the model calibration was successful with an  $R^2 > 0.75$  for all the spectral classes, except 400-440nm class where the model was crushing. On validating the method the correlation between the in-situ and derived  $K_d(\lambda)$  was high across the spectral classes. However, the 600-800nm range had the lowest correlation ( $R^2 = 0.8$ ). The most accurate was 800-930nm which gave the lowest RMSE and relative mean error. The low correlation in the spectral class 2 could be attributed to the fact that relationship between  $K_d(\lambda)$  and  $R_{rs}(\lambda)$  in this range is not well defined like the other two classes that show a clear relationship, as illustrated in Figure 5-1.

### 6.3. Mapping $Z_{eu}$

The first step to accurate derivation of optical water properties from satellite data is to remove the effect of the atmosphere from the total radiance recorded by the sensor. Because only MERIS match-up data was used for this study, atmospheric correction was performed by subtracting in-situ water-leaving reflectances from reflectances recorded by the sensor to determine the atmospheric path. The resultant atmospheric path was subtracted from the MERIS top-of-atmosphere reflectance to give the water-leaving reflectances from the images, which was used for validating the  $K_d(\lambda)$  model and producing maps. This method was successful in retrieving the remote sensing reflectances on all images as indicated by the statistical analysis techniques presented in Table 5-2. The in-situ validated  $K_d$  model was then applied on these products and tested for accuracy. The results were satisfactory, except for the image of 17/09/2010, which reported the highest RMSE values on all spectral classes. 800-930nm class gave the lowest accuracy on all the images ( $RMSE > 1.7m^{-1}$ ). 600-800nm range, in contrast had the lowest RMSE ( $< 0.2m^{-1}$ ), and  $R^2$  ( $< 0.85$ ).

For deriving  $Z_{eu}$  from MERIS, the empirical  $K_d(490)$  and  $K_d(620)$  models that were developed were applied on the  $K_d$  products.  $K_d(490)$  has been used before to develop a local model for retrieving  $Z_{eu}$  from remote sensing data (Kratzer et al., 2003; Tang et al., 2007). However in this research the  $K_d(620)$ -derived  $Z_{eu}$  was more accurate than the  $K_d(490)$ -derived  $Z_{eu}$ . The regression analysis gave a slope of almost 1 for  $K_d(PAR)/K_d(620)$  relationship, showing higher correlation between the two values. For  $K_d(PAR)/K_d(490)$ , although the relationship was linear, the value of  $K_d(PAR)$  was almost twice that of  $K_d(490)$ .

The atmospheric correction results show very high correlation ( $R^2 > 0.9$ ) for all the images.

The  $Z_{eu}$  in the lake generally ranges between 0.9 and 1.3m, as shown in the maps. The empirical method derived  $Z_{eu}$  is highest at the Crescent Island Lake across the three maps. This was explained by the fact that water on that part of the lake is clearer than the main lake, thus deeper light penetration. At the main lake, however,  $Z_{eu}$  varies between 0.9m and 1.13m. The northern part of the lake also showed high  $Z_{eu}$  although this is where the inlet of the rivers are found (Figure 3-2) (Odada et al., 2006). The river water is high in suspended load, causing water to be turbid, thus the expected result was high attenuation of radiation and low  $Z_{eu}$ . This could be explained by the presence of the aquatic plants in that region that resulted in high reflectances. On all the days, however, it can be observed that  $Z_{eu}$  is generally uniform across the whole lake.

### 6.4. Limitations

Various factors contributed to the errors experienced in this research. The modelling approach is currently not being applied, thus various assumptions were also made during developing of the model.

- The weather conditions were adverse in some days during field measurements, such that it was a challenge to accurately collect data
- Atmospheric correction method was very good, but not 100% accurate. The error generated here contributed to the total error of the derived  $K_d(\lambda)$
- The error propagated at each model development stage contributed to the final error in the  $Z_{eu}$
- The difference in spatial resolution between in-situ measurements and MERIS data. 300m spatial resolution MERIS was used, whereas the field measurements characterise an area of 1-10m<sup>2</sup>. The uncertainty introduced here is hard to quantify
- One big limitation for analysing temporal variation of  $Z_{eu}$  was the difficulty in finding cloud free images of the lake.



## 7. CONCLUSIONS AND RECOMMENDATIONS

### 7.1. Conclusions

The main aim of this study was to derive  $Z_{eu}$  from remote sensing data by first modelling  $K_d(\lambda)$  from in-situ measurements. Therefore the following conclusions were made:

- There is a defined inverse relationship between  $K_d(\lambda)$  and  $R_{rs}(\lambda)$ , which was exploited when the model was developed. The research was thus able to distinctly split the spectra into 3 classes based on this relationship
- The  $K_d(\lambda)$  model that was developed worked well in deriving  $K_d(\lambda)$  from MERIS data in all the spectral ranges, as evidenced by the high correlation during validation
- $Z_{eu}(\lambda)$ , was retrieved from radiometric measurements of underwater downwelling irradiance at two depths and the exponential relationship between depth and  $K_d(\lambda)$ . The results showed a distinct peak at 705nm that was caused by the high concentration of chlorophyll in the lake
- Because of high accuracy in retrieving  $K_d(\lambda)$  from the MERIS imagery, it was possible to produce very accurate maps of PAR  $Z_{eu}$  using a local algorithm that was developed from regression of  $K_d(\text{PAR})$  against  $K_d(620)$ . The maps show a general spatial uniformity of euphotic depth across the lake. The Crescent lake waters have higher light penetration than the main lake
- From the spatial analysis, it can be noted that there are two water types in the lake, the clearer Crescent Island water, that has deeper light depth
- The in-situ data collected at the lake will go a long way in calibration and validation of inland water models.

### 7.2. Recommendations

- Since this methodology of modelling  $K_d(\lambda)$  from  $R_{rs}(\lambda)$  has not been exploited much, it needs to be tested at various water environments. As a new methodology, it has only been tested using radiometric data from Naivasha Lake. Since it was only validated on MERIS data, its usability also has to be tested in other satellite data
- To improve the accuracy during data collection, the sampling strategies should follow specified protocols and standard procedure precisely, some depicted by NASA (2003). This will reduce uncertainties and error introduced during data collection
- More accurate atmospheric correction methods must be applied to reduce the error on the final product of remotely sensed data
- Spectral data merging would help further when one wants to do trend and temporal analysis of light penetration in the lake. This would be very helpful to also incorporate the effect of climate change and/ or environmental degradation on the light status of the lake
- Since underwater light attenuation is influenced by IOP's, these should be studied together to understand their relationships further.



## LIST OF REFERENCES

---

- Austin, R. & Petzold, T. (1981). The determination of the diffuse attenuation coefficient of sea water using the Coastal Zone Color Scanner. *Oceanography from space*, 239-256.
- Barnard, A. H., Zaneveld, J. R. V., Pegau, W. S., Mueller, J. L., Maske, H., Lara-Lara, R. et al. (1999). The determination of PAR levels from absorption coefficient profiles at 490 nm *Ciencias Marinas*, 25(4), 487-507.
- Becht, R. & Chesterton, M. (2010). Flower farming from a hydrologist's perspective : are Marnie's roses, and the other millions of romantic bouquets, really responsible for draining the water of Lake Naivasha and polluting it with pesticides and fertilizer? Available from [http://download.omroep.nl/rnw/smac/cms/robert\\_becht\\_hydrologist\\_20100211\\_44\\_1kHz.mp3](http://download.omroep.nl/rnw/smac/cms/robert_becht_hydrologist_20100211_44_1kHz.mp3), [http://intranet.itc.nl/papers/2010/pres/becht\\_flo.mp3](http://intranet.itc.nl/papers/2010/pres/becht_flo.mp3)
- Bilotta, G. S. & Brazier, R. E. (2008). Understanding the influence of suspended solids on water quality and aquatic biota. *Water Research*, 42(12), 2849-2861.
- Chen, J., Shang, S., Tang, J., Lee, Z., Hong, H., Dai, M. et al. (2007). A test of empirical and semi-analytical algorithms for euphotic zone depth with SeaWiFs data off southeastern China. *Coastal Ocean Remote Sensing*, 6680(17), 1-10.
- Chomko, R. M. & Gordon, H. R. (2001). Atmospheric Correction of Ocean Color Imagery: Test of the Spectral Optimization Algorithm with the Sea-Viewing Wide Field-of-View Sensor. *Appl. Opt.*, 40(18), 2973-2984.
- DiGiacomo, P., Hook, S., Neumann, A., Groom, S., Hoepffner, N., Dowell, M. et al. (2007). *GEO Inland and Nearshore Coastal Water Quality Remote Sensing Workshop*.
- ESA. (2006). MERIS Product Handbook (pp. 130): European Space Agency.
- Fathy, A. H., Gieske, A. S. M. & Meijerink, A. M. J. (1999). *Time series analysis of NOAA - AVHRR images of lake Naivasha basin, Kenya*. Paper presented at the 2nd international conference on operationalisation of remote sensing, August 16-20, 1999. Enschede, The Netherlands. 10 p.
- Gitelson, A. (1992). The peak near 700 nm on radiance spectra of algae and water: relationships of its magnitude and position with chlorophyll concentration. *International Journal of Remote Sensing*, 13(17), 3367-3373.
- Gitelson, A. A., Schalles, J. F., Rundquist, D. C., Schiebe, F. R. & Yacobi, Y. Z. (1999). Comparative reflectance properties of algal cultures with manipulated densities. *Journal of Applied Phycology*, 11(4), 345-354.
- Goosen, N. K., Kromkamp, J., Peene, J., van Rijswijk, P. & van Breugel, P. (1999). Bacterial and phytoplankton production in the maximum turbidity zone of three European estuaries: the Elbe, Westerschelde and Gironde. *Journal of Marine Systems*, 22(2-3), 151-171.
- Han, L. (1997). Spectral reflectance with varying suspended sediment concentrations in clear and algae-laden waters. *Photogrammetric Engineering and Remote Sensing*, 63(6), 701-705.
- Han, L. & Rundquist, D. C. (1997). Comparison of NIR/RED ratio and first derivative of reflectance in estimating algal-chlorophyll concentration: a case study in a turbid reservoir. *Remote Sensing of Environment*, 62(3), 253-261.
- Harper, D. M. (1993). Eutrophication prognosis for lake Naivasha, Kenya. *Proceedings of the international association of theoretical and applied limnology*, 25(2), 861-865.
- Harper, D. M., Adams, C. & Mavuti, K. (1995). The aquatic plant communities of the Lake Naivasha wetland, Kenya: pattern, dynamics and conservation. *Wetlands Ecology and Management*, 3(2), 111-123.
- Harper, D. M., Boar, R. R., Everard, M. & Hickey, P. (2003). *Lake Naivasha, Kenya : papers from the conference: Science and the sustainable management of Shallow Tropical waters, Naivasha, Kenya, 11 - 16 April 1999 + additional studies on the lake*. Dordrecht etc.: Kluwer Academic.
- Holtz, U. & Tanya, S. (2007). Introductory Digital Image Processing: A Remote Sensing Perspective. *Environmental and Engineering Geoscience*, 13(1), 89.
- Jimoh, H. E., Vogler, C. & Waters, J. J. J. (2007). Perceived and real sources of pollution in Lake Naivasha Tropical Biology Association.
- Kahru, M., Leppanen, J. M. & Rud, O. (1993). Cyanobacterial Blooms cause Heating of the Sea-surface. *Marine Ecology-Progress Series*, 101(1-2), 1-7.
- Kettle, H. & Merchant, C. J. (2008). Modeling ocean primary production: Sensitivity to spectral resolution of attenuation and absorption of light. *Progress in Oceanography*, 78, 135-146.

- Khanna, D. R., Bhutiani, R. & Chandra, K. S. (2009). Effect of the Euphotic Depth and Mixing Depth on Phytoplanktonic Growth Mechanism. *International Journal of Environmental Resources*, 3(2), 223-228.
- Kirk, J. T. O. (1994). *Light and Photosynthesis in Aquatic Ecosystems*, 2nd edition. Cambridge: Cambridge University Press.
- Kona, E. & Mwititi, C. (2010). Mysterious disease kills fish in L. Naivasha. *Kenya Broadcasting Cooperation*.
- Kratzer, S., Brockmann, C. & Moore, G. (2008). Using MERIS full resolution data to monitor coastal waters -- A case study from Himmerfjärden, a fjord-like bay in the northwestern Baltic Sea. *Remote Sensing of Environment*, 112(5), 2284-2300.
- Kratzer, S., Håkansson, B. & Charlotte, S. (2003). Assessing Secchi and Photic Zone Depth in the Baltic Sea from Satellite Data. *Remote Sensing for the Environment*, 32 (8), 577-585
- Lee, Z., Darecki, M., Carder, K. L., Davis, C. O., Stramski, D. & Rhea, W. J. (2005a). Diffuse attenuation coefficient of downwelling irradiance: An evaluation of remote sensing methods. *Journal of Geophysical Research*, 110.
- Lee, Z., Du, K., Arnone, R., Liew, S. & Penta, B. (2005b). Penetration of solar radiation in the upper ocean: A numerical model for oceanic and coastal waters. *J. Geophys. Res.*, 110(C9), C09019.
- Lee, Z., Weidemann, A., Kindle, J., Arnone, R., Carder, K. L. & Davis, C. (2007). Euphotic zone depth: Its derivation and implication to ocean-color remote sensing. *Journal of Geophysical Research-Oceans*, 112(C3).
- Lewis, M. R., Carr, M.-E., Feldman, G. C., Esaias, W. & McClain, C. (1990). Influence of penetrating solar radiation on the heat budget of the equatorial Pacific Ocean. *Nature*, 347(6293), 543-545.
- Liu, C. C. (2006). Fast and accurate model of underwater scalar irradiance for stratified Case 2 waters. *Optics Express*, 14(5), 1703-1719.
- Liu, C. C., Carder, K. L., Miller, R. L. & Ivey, J. E. (2002). Fast and accurate model of underwater scalar irradiance. *Applied Optics*, 41(24), 4962-4974.
- Loisel, H. & Stramski, D. (2000). Estimation of the inherent optical properties of natural waters from the irradiance attenuation coefficient and reflectance in the presence of Raman scattering. *Applied Optics*, 39(18), 3001-3011.
- Lozano-Rivera, P. (2009). *Mapping suspended sediment concentration using the diffuse attenuation coefficient  $K_d$  and multi spectral and spatio temporal images in Caribbean coastal waters of Colombia*. ITC, Enschede.
- Malone, T. C. (1987). Primary production of the ocean water column as a function of surface light intensity. *Deep Sea Research Part A. Oceanographic Research Papers*, 34(1), 139-139.
- Manizza, M., Le Quere, C., Watson, A. J. & Buitenhuis, E. T. (2004). Bio-optical feedbacks among phytoplankton, upper ocean physics and sea-ice in a global model. *Geophysical Research Letters*.
- Maseck, J. (2010). Data Products *Landsat 7 Science Data Users Handbook*. Maryland: NASA.
- Microbiologyprocedure.com. from <http://www.aquatic.uoguelph.ca/lakes/page21.htm>
- Mobley, C. D. (2004). *Light and Water: Radiative Transfer in Natural Waters*: Elsevier Science & Technology Books.
- Morel, A. & Antoine, D. (1994). Heating Rate withing the Upper Oceanin Relation to Its Bio-Optical State. *Journal of Physical Oceanography*, 24, 1652– 1665.
- Morel, A. & Berthon, J.-F. (1989). Surface Pigments, Algal Biomass Profiles, and Potential Production of the Euphotic Layer: Relationships Reinvestigated in View of Remote-Sensing Applications. *Limnology and Oceanography*, 34(8), 1545-1562.
- Morel, A. & Maritorena, S. (2001a). Bio-optical properties of oceanic waters: A reappraisal. *Journal of Geophysical Research*, 106(C4), 7163-7180.
- Morel, A. & Maritorena, S. (2001b). Bio-optical properties of oceanic waters: a reappraisal. *J. Geophys. Res.*, 106(C4), 7163-7180.
- Mueller, J. (2000). SeaWiFS algorithm for the diffuse attenuation coefficient,  $K(490)$ , using water-leaving radiances at 490 and 555 nm. *SeaWiKS Postlaunch Calibration and Validation Analyses. NASA Tech. Memo*, 206892, 11-24.
- Mueller, J. L. & Lange, R. E. (1989). Bio-optical provinces of the northeast Pacific Ocean: a provisional analysis. *Limnology and Oceanography*, 34(8), 1572-1586.
- Mueller, J. L., Morel, A., Frouin, R., Davis, C., Arnone, R., Carder, K. et al. (2003a). Ocean Optics Protocols For Satellite Ocean Color Sensor Validation, Revision 4, Volume III: Radiometric Measurements and Data Analysis Protocols.
- Mueller, J. L., Morel, A., Frouin, R., Davis, C., Arnone, R., Carder, K. et al. (2003b) Ocean Optics Protocols For Satellite Ocean Color Sensor Validation, Revision 4, Volume IV: Inherent Optical

- Properties: Instruments, Characterizations, Field Measurements and Data Analysis Protocols. National Aeronautical and Space Administration.
- NASA. (2003). Ocean Optics Protocols For Satellite Ocean Color Sensor Validation, Volume III, *Radiometric Measurements and Data Analysis Protocols* (pp. 78). Greenbelt, Maryland: Goddard Space Flight Space Center.
- O'Reilly, J. E., Maritorena, S., Mitchell, B. G., Siegel, D. A., Carder, K. L., Garver, S. A. et al. (1998). Ocean color chlorophyll algorithms for SeaWiFS. *J. Geophys. Res.*, 103(C11), 24937-24953.
- Odada, E. O., Higgins, S. & Becht, R. (2006). *Lake Naivasha: Experience and Lessons Learned Brief*. Naivasha: University of Kenya.
- Otien'a-Owiti, G. E. & Abiya Oswe, I. (2006). Human impact on lake ecosystems : the case of Lake Naivasha, Kenya. In: *African journal of aquatic science*, 32(2007)1, pp. 79-88.
- Phlips, J., Lynch, T. C. & Badylak, S. (1995). Chlorophyll a, tripton, color, and light availability in a shallow tropical inner-shelf lagoon, Florida Bay, USA. *Marine Ecology Progress Series*, 127, 223–234.
- Platt, T., Sathyendranath, S., Caverhill, C. M. & Lewis, M. R. (1988). Ocean primary production and available light: further algorithms for remote sensing. *Deep Sea Research Part A. Oceanographic Research Papers*, 35(6), 855-879.
- Randolph, K. L. (2007). *Remote sensing of cyanobacteria in case II waters using optically active pigments, chlorophyll a and phycocyanin*. faculty of the University Graduate School in partial fulfillment of the requirements for the degree Master of Science in the Department of Geography, Indiana University.
- Scheffer, M. (2001). *Ecology of Shallow Waters* (2nd ed.). Dordrecht: Kluwer Academic Publishers
- Schwartz, E., DeBuhr, L. & Addelson, B. (2002). Ocean Light Zones. from [www.mbgnet.net/salt/oceans/zone.htm](http://www.mbgnet.net/salt/oceans/zone.htm)
- Spitzer, D. (1980). Efficiency of Primary Production in the Upper Layer of the Euphotic Zone of the Tropical North Atlantic. *Netherlands Journal of Sea Research*, 14 (2), 220-228
- Stavn, R. & Weidemann, A. (1989). Shape factors, two-flow models, and the problem of irradiance inversion in estimating optical parameters. *Limnology and Oceanography - JSTOR*, 34(8), 1426-1441.
- Tang, S., Chen, C., Zhan, H. & Xu, D. (2007). Remotely-sensed estimation of the euphotic depth in the northern South China Sea. *IEEE*.
- Zaneveld, J. R. V., Kitchen, J. C. & Mueller, J. L. (1993). Vertical structure of productivity and its vertical integration as derived from remotely sensed observations. *Limnology and Oceanography*, 38(7), 1384-1393.
- Zhang, Y., Qin, B., Hu, W., Wang, S., Chen, Y. & Chen, W. (2006). Temporal-spatial variations of euphotic depth of typical lake regions in Lake Taihu and its ecological environmental significance. *Science in China Series D: Earth Sciences*, 49(4), 431-442.